Available online at www.sciencedirect.com
ScienceDirect
Comput. Methods Appl. Mech. Engrg. 414 (2023) 116195
Computer methods in applied mechanics and engineering
www.elsevier.com/locate/cma

Signed distance field enhanced fully resolved CFD-DEM for simulation of granular flows involving multiphase fluids and irregularly shaped particles

Zhengshou Lai[a,b,d,*], Jidong Zhao[b,c,**], Shiwei Zhao[b], Linchong Huang[a,d]

[a] School of Civil Engineering, Sun Yat-Sen University, Zhuhai 519082, China
[b] Department of Civil and Environmental Engineering, The Hong Kong University of Science and Technology, Hong Kong, China
[c] HKUST Shenzhen-Hong Kong Collaborative Innovation Research Institute, Shenzhen 518045, China
[d] School of Aeronautics and Astronautics, Shenzhen Campus of Sun Yat-sen University, Shenzhen 518000, China

Received 7 December 2022; received in revised form 15 June 2023; accepted 16 June 2023
Available online 7 July 2023

Abstract

It is challenging to model granular particles with arbitrary shapes and related complications to fluid–particle interactions for granular flows which are widely encountered in nature and engineering. This paper presents an improved framework of the immersed boundary method (IBM)-based fully resolved computational fluid dynamics (CFD) and discrete element method (DEM), with an emphasis on irregular-shaped particles and the implications to particle–fluid interactions. The improved CFD-DEM framework is featured by two novel enhancements with signed distance field (SDF). First, an SDF-based formulation is employed to enable handling of granular particles with arbitrary shapes in DEM robustly and efficiently. Second, the IBM is modified to be consistent with SDF to fully resolve fluid–particle interactions in the presence of non-spherical particles. Such treatments leverage SDF as a generic interface to furnish a new SDF-CFD-DEM framework for universal modeling of arbitrarily shaped particles interacting with multiphase fluids with desired resolutions. Exemplified particle shape models include super-quadrics, spherical harmonics, polyhedron and level set, and new shape models can be flexibly developed by implementing the unified SDF-based shape interface. The proposed SDF-CFD-DEM is validated and showcased with examples including particle settling, drafting–kissing–tumbling, immersed granular collapse, and mudflow. The results demonstrate the good accuracy and robustness of the SDF-CFD-DEM and its potential for efficient computational modeling of multiphase granular flows involving granular particles with arbitrary shapes.

Keywords: CFD-DEM; Irregular-shaped; Multiphase; Immersed boundary; Signed distance field

1. Introduction

Fluid–particle systems are common in nature and important to engineering practice. They may present in forms of geophysical flows such as debris and mud flows [1], internal erosion of earth dams [2], rock armor offshore

* Corresponding author at: School of Civil Engineering, Sun Yat-Sen University, Zhuhai 519082, China.
** Corresponding author at: Department of Civil and Environmental Engineering, The Hong Kong University of Science and Technology, Hong Kong, China.
E-mail addresses: laizhengsh@email.sysu.edu.cn (Z. Lai), jzhao@ust.hk (J. Zhao).

https://doi.org/10.1016/j.cma.2023.116195
0045-7825/

projection [3], wave induced breakage and transport of coral sand [4], and particle mixing and reaction in fluidized bed [5]. The behavior of a fluid–particle system depends on both the particles and the constituent fluids, and more critically on the interactions between particles and fluids. On one hand, fluids and fine particles can flow through a heterogeneously structured porous granular packing where the shape of individual particle and the pore structure play a decisive role in the flow behavior. There are many types of fluid–particle interactions (e.g., buoyant, drag, capillary force, surface tension) [6–8], which are under the influence of combined factors including fluid velocity, particle shape and solid volume fraction. The behavior of fluid–particle systems is essentially encoded at the microscopic scale, where the complex fluid–particle interactions originating from both the fluids and the particles may not be fully captured by current experimental measurements. Numerical modeling has become an important tool for understanding and predicting the behavior of fluid–particle systems.

Most numerical approaches treat the motion of fluids by solving the so-called Navier–Stokes equations [9]. Numerical methods for computational fluid dynamics (CFD) include finite volume method (FVM) [10], finite element method (FEM) [11], finite difference method (FDM) [12], lattice Boltzmann method (LBM) [13], smoothed particle hydrodynamics (SPH) [14]. Among these methods, FVM is a Euler-based approach convenient to describe the motion of fluids and is adopted by many CFD software packages, including the widely used open-source code *OpenFOAM* [15]. LBM and SPH are based on Lagrangian description and have been used in open-source libraries such as *Palabos* [16] and *DualSPHysics* [17]. For numerical modeling of particles, the discrete element method (DEM) [18] has been one of the most popular approaches with wide applications across many engineering disciplines (e.g., [19–22]). In DEM, all individual particles are explicitly modeled based on the Newton-Euler equation to resolve the interparticle interactions in a direct manner. The bulk behavior of a granular material is presented as an assembly of the actions (i.e., the interactions and motions) of all constituent particles. The CFD method and DEM can be combined into a coupled CFD-DEM representation of a fluid–particle system.

Depending on the modeling resolution of fluid and the relative size of particles, the CFD-DEM methods can be categorized into an unresolved approach [7,23–26] and a resolved one [27–33]. In the unresolved approach, the force applied onto particles by fluids is characterized by empirical equations such as the drag force models [34,35], whereas the force exerted on the fluids by particles is determined from the reaction force or characterized by the Darcy's law. To ensure sufficient accuracy, the fluid mesh should be about three times greater than the particle size [36], making it suitable for large fluid–particle systems with a coarse-scale modeling of fluid and fluid–particle interaction. For fine-scale modeling, the resolved method shall be used to solve fluid–particle interactions directly and fully. A conventional option for resolved CFD-DEM is the body-conformal Arbitrary Lagrangian-Eulerian method [37]. It utilizes a moving, unstructured, finite-element mesh to deal with the movement of particles, which may suffer from numerical instability due to the severe distortion of mesh as the particles move and thus may require frequent mesh reconstruction. A promising alternative is the immersed boundary method (IBM), which is originally proposed by Peskin [38] and has been well developed and successfully applied to simulate a variety of complex fluid–particle coupled problems [27–33]. IBM considers the fluid domain as a complete and fixed grid with the particles immersed into it. The influence of particle motion on the fluid is accounted for by adding a source term to the governing equations of the fluid.

In fluid–particle systems, particles are often non-spherical in nature. Particle irregularity has been well recognized to have substantial effects on the macroscopic properties, such as the packing density, stiffness and strength, of a granular medium [39]. There have been attempts to incorporate arbitrary-shaped objects/particles in the IBM-based resolved CFD-DEM over the years [40,41]. For example, Galindo-Torres [42] developed a sphero-polyhedron technique to model generally shaped particles in LBM-DEM. Wang et al. [43] introduced a polygonal LBM-DEM approach with an energy-conserving contact algorithm. Zhang and Tahmasebi [44,45] proposed an image-based DEM and integrated it with CFD for coupled modeling of single-phase fluid and irregular particles. These approaches could be either memory demanding or computationally expensive in handling irregular-shaped particles in DEM, limiting their application to large granular systems. Multi-sphere clump-particle approach has also been used to model irregular-shaped particle in DEM [46] for resolved CFD-DEM coupling [47]. The clump-particle approach has the disadvantages of low computational efficiency and unrealistic contact parameters [48,49].

It is highly desirable to develop a versatile particle modeling strategy that can accurately accommodate the various shape features of particles while offering the best computational efficiency. Such a model should also ideally facilitate the computing of fluid–particle interaction for optimal performance. To approach this goal, we employ a signed distance field (SDF) approach we recently developed for modeling generic irregular-shaped particles [50].

The SDF-DEM is an extension of the level set-based DEM (LS-DEM) [51] enhanced by two important features. First, the particle models in SDF-DEM all inherit from a generic SDF-based particle interface, rendering it easy to accommodate various classical geometries, such as poly-super-ellipsoid, poly-super-quadrics, spherical harmonics, polyhedron. These geometries are specialized in modeling typical granular materials and could be flexibly adopted to pursue desired optimal performance in terms of memory consumption and computational efficiency. For example, spherical harmonics is widely used to characterize irregular-shaped particles and to create new virtual particles [52]. Spherical harmonics is directly palatable to the SDF-DEM, while showing lower memory consumption comparing with the grid-based LS-DEM. Second, the contact behavior is derived from an extended node-based energy-conserving contact theory, which is significantly beneficial to numerical stability and enables quantitative energy analysis of a DEM simulation. With the energy-conserving contact theory, various complex contact behaviors, including the classical linear spring model and Hertz model, could be rigorously reproduced by formulating the contact potential in a physically meaningful manner.

The main focus of this work will be placed to integrate the SDF-DEM with CFD to offer a new efficient and flexible option for numerical modeling of fluid–particle systems consisting of multiphase fluids and irregular-shaped granular materials. Note that an interesting SDF-based discrete forcing IBM has recently been presented by Zhang [53]. However, it does not contain a strong ingredient of DEM for rigorous modeling of fluid–particle systems. The rest of the paper is organized as follows. Section 2 describes the methodologies of the resolved SDF-CFD-DEM, including the formulations of CFD, SDF-DEM and IBM. Section 3 discusses about the numerical aspects and implementation. Section 4 presents the verification tests and Section 5 presents several illustrative examples to further showcase the capabilities of the SDF-CFD-DEM. Finally, Section 6 summarizes the concluding remarks.

2. Methodology of the resolved SDF-CFD-DEM

In the resolved SDF-CFD-DEM, the volume of fluid (VOF) method is employed to model multiphase fluids and the interface between two phases [54]. For DEM, the SDF-based DEM [50] recently proposed by the authors is adopted. The SDF-DEM is applicable to arbitrarily shaped particles and covers most particle models (including poly-super-quadrics, spherical harmonics, polyhedron, level set) as special cases. Importantly, the same umbrella of SDF renders it flexible and efficient to be integrated with CFD as detailed below. To deal with the interaction between fluid and particle, the IBM approach is employed. The formulations of multiphase CFD, SDF-DEM and the IBM-based fluid–particle interaction are presented in the following.

2.1. Formulation of multiphase CFD

For simplicity, this work considers two-phase incompressible fluids. The continuity and momentum equations are given

$$\nabla \cdot \boldsymbol{u}_f = 0 \tag{1}$$

$$\frac{\partial(\rho_f \boldsymbol{u}_f)}{\partial t} + \nabla \cdot (\rho_f \boldsymbol{u}_f \otimes \boldsymbol{u}_f) = -\nabla p + \nabla \cdot (\mu_f \nabla \otimes \boldsymbol{u}_f) + \rho_f \boldsymbol{g} + \boldsymbol{f}_t + \boldsymbol{f}_{IB} \tag{2}$$

where $\boldsymbol{u}_f$ is the fluid velocity, p is the pressure, ρ_f is fluid density, μ_f is dynamic viscosity, $\boldsymbol{g}$ is the gravitational coefficient, $\boldsymbol{f}_t$ represents the surface tension force at phase interface and $\boldsymbol{f}_{IB}$ represents the interaction force from solid particles based on IBM.

In the VOF method, the combined density and viscosity of two-phase fluids are calculated as

$$\rho_f = \alpha_1 \rho_1 + \alpha_2 \rho_2 \tag{3}$$

$$\mu_f = \alpha_1 \mu_1 + \alpha_2 \mu_2 \tag{4}$$

where ρ_1, ρ_2, μ_1 and μ_2 are the density and viscosity of phase 1 fluid and phase 2 fluid, respectively; and, α_1 and α_2, respectively, are the volume fractions of phase 1 and 2 fluids, with $\alpha_1 + \alpha_2 = 1$. An additional transport equation for VOF is written as

$$\frac{\partial \alpha_1}{\partial t} + \nabla \cdot (\alpha_1 \boldsymbol{u}_f) = \nabla \cdot (\Gamma \nabla \alpha_1) \tag{5}$$

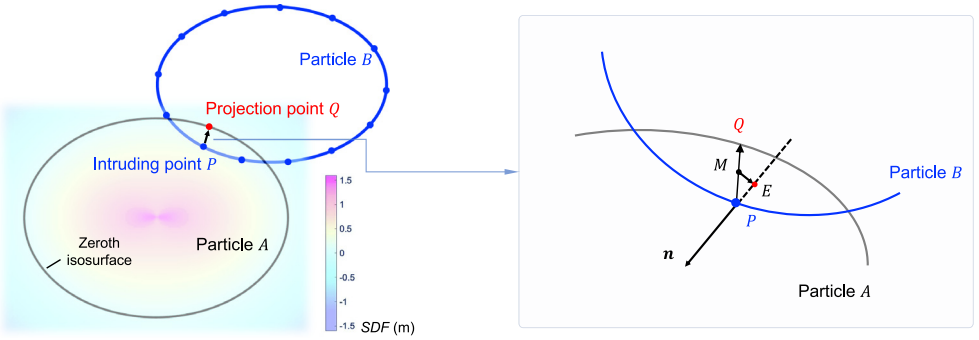

Fig. 1. Illustration of particle description, contact detection and contact resolution in the SDF-DEM.

where the term $\nabla \cdot (\Gamma \nabla \alpha_1)$ accounts for the diffusivity of the fluid shapes and could be taken as 0 for immiscible fluids [27]. The surface tension force $\boldsymbol{f}_t$ is calculated as

$$\boldsymbol{f}_t = \sigma \kappa \nabla \alpha_1 \tag{6}$$

where σ is the surface tension coefficient, κ is the surface curvature.

2.2. Formulation of SDF-DEM

The SDF-DEM was recently proposed by the authors with the applicability to arbitrary-shaped particles. The formulation of SDF-DEM is briefly described herein for the sake of completeness, whereas interested readers are referred to [50] for more details. In DEM, the particle motion is governed by the Newton-Euler equation as

$$m\frac{\partial \boldsymbol{u}_p}{\partial t} = m\boldsymbol{g} + \boldsymbol{F}_c + \boldsymbol{F}_f \tag{7}$$

$$\boldsymbol{I}\frac{\partial \boldsymbol{\omega}_p}{\partial t} + \boldsymbol{\omega}_p \times (\boldsymbol{I}\boldsymbol{\omega}_p) = \boldsymbol{M}_c + \boldsymbol{M}_f \tag{8}$$

where $\boldsymbol{u}_p$ and $\boldsymbol{\omega}_p$ are the particle translation and rotation velocities, respectively; m and $\boldsymbol{I}$ are the particle mass and moment of inertia tensor, respectively; and $\boldsymbol{F}_c$, $\boldsymbol{M}_c$, $\boldsymbol{F}_f$ and $\boldsymbol{M}_f$, respectively, are the contact force, contact moment, fluid force and force moment subjected by the particle.

In the SDF-DEM [50], particles are described using an SDF-based generic interface furnished with two functions, namely the SDF function and surface projection function. As illustrated in Fig. 1, the SDF function maps a location to a scalar, which is assumed to be positive for locations inside a particle and negative outside. Thus, the zeroth isosurface of SDF represents the particle surface. The surface projection function projects a point onto the surface of the particle and is used to determine the contact point. Formulations of example particle models (e.g., super-ellipsoid, spherical harmonics, and polyhedron) could be found in Lai et al. [50]. With the SDF-based particle description, the node-to-surface contact algorithm is adopted to detect contacts and resolve contact geometric features. The contact detection thus becomes to test if any surface node on Particle B intrudes into Particle A. The corresponding contact point (e.g., point E in Fig. 1) is defined as the projection of the middle of an intruding point and its surface projection onto the contact normal line passing the intruding point.

For contact resolution, the SDF-DEM employs the energy-conserving contact theory to enhance the numerical stability [55]. Based on this contact theory, the contact normal force is computed from the derivatives of a contact potential function with respect to particles' relative translation and rotation, as

$$\boldsymbol{F}_n = -\frac{\partial w(\boldsymbol{x}, \boldsymbol{\theta})}{\partial \boldsymbol{x}} \tag{9}$$

$$\boldsymbol{M}_n = -\frac{\partial w(\boldsymbol{x}, \boldsymbol{\theta})}{\partial \boldsymbol{\theta}} \tag{10}$$

where $\boldsymbol{F}_n$ and $\boldsymbol{M}_n$ are the normal contact force and moment, respectively, $w(\boldsymbol{x}, \boldsymbol{\theta})$ denotes the contact potential, and $\boldsymbol{x}$ and $\boldsymbol{\theta}$ represents the relative position and rotation of particle B with respect to particle A. The formulation of a

linear contact potential is presented in Appendix. To further account for the tangential frictional force, the classical linear spring contact model with Coulomb friction law is adopted. The contact tangential force is updated in an incremental manner, as

$$F_s = F_s^0 - k_t \delta_s \tag{11}$$

$$F_t = F_t^0 - k_t \delta_t \tag{12}$$

where F_s and F_t are the tangential contact forces in the tangential directions $\boldsymbol{s}$ and $\boldsymbol{t}$, respectively; the superscript 0 indicates the tangential forces at the previous timestep; k_t is the contact tangential stiffness; and δ_s and δ_t, respectively, are the relative displacements in the contact tangential directions. And, by incorporating the Coulomb's law of friction [56,57], the tangential contact forces are constrained as

$$F'_{st} = \min\left(\sqrt{F_s^2 + F_t^2}, \mu F_n\right) \tag{13}$$

$$F'_s = F'_{st} \frac{F_s}{\sqrt{F_s^2 + F_t^2}} \tag{14}$$

$$F'_t = F'_{st} \frac{F_t}{\sqrt{F_s^2 + F_t^2}} \tag{15}$$

where the symbol prime $'$ is used to indicate the updated tangential contact force based on the Coulomb's law of friction, F_{st} is the total tangential contact force, and μ is the friction coefficient.

It is worth noting that each intruding node will carry a contact force, and thus the total contact force needs to be added up from all the intruding nodes of two colliding particles. Thereby, the total contact force and moment are computed as

$$\boldsymbol{F}_c = \sum^{P_i} \left(\boldsymbol{F}_n + F'_s \boldsymbol{s} + F'_t \boldsymbol{t}\right) \tag{16}$$

$$\boldsymbol{M}_c = \sum^{P_i} \left(\boldsymbol{M}_n + F'_s \boldsymbol{b} \times \boldsymbol{s} + F'_t \boldsymbol{b} \times \boldsymbol{t}\right) \tag{17}$$

where $\boldsymbol{b}$ is the branch vector from particle centroid to contact point, $\boldsymbol{s}$ and $\boldsymbol{t}$ are the contact tangential directions, respectively, and $\sum^{P_i}$ indicates a summation for all the surface nodes that intrude into another particle.

2.3. IBM approach for fluid–particle interaction

The IBM approach assumes that there exists a fictitious CFD domain at the space occupied by the DEM particles. In particular, this work adopts the volume fraction-based IBM [58,59]. The forces from fluids to particles are evaluated based on the IBM approach and are applied as an external force onto the particles; and, the forces from particles to fluids are accounted for by added a source force to the Navier–Stokes momentum equation at the mesh cell centers. To account for the influence of particles, the fluid density is first corrected to a combined density [60]

$$\rho = (1 - \phi_s)\rho_f + \phi_s \rho_s \tag{18}$$

where ρ_s is the particle density, and ϕ_s is the cell solid fraction and its calculation will be described in a subsequent section. An IBM-related source force $\boldsymbol{f}_{IB}$ is then imposed on the fluid so that the fluid overlapped by particles would have the same velocity as the particles. As illustrated in Fig. 2, for the fluid cells overlapped by particles, the fluid velocity needs to be corrected to

$$\hat{\boldsymbol{u}}_f = (1 - \varphi_s)\boldsymbol{u}_f + \varphi_s \boldsymbol{u}_s \tag{19}$$

where $\varphi_s = \phi_s \rho_s / \rho$ represents the density weighted solid fraction, and $\boldsymbol{u}_s$ represents solid velocity interpolated at the cell center and is calculated as

$$\boldsymbol{u}_s = \boldsymbol{u}_p + \boldsymbol{\omega}_p \times (\boldsymbol{x}_i - \boldsymbol{x}_p) \tag{20}$$

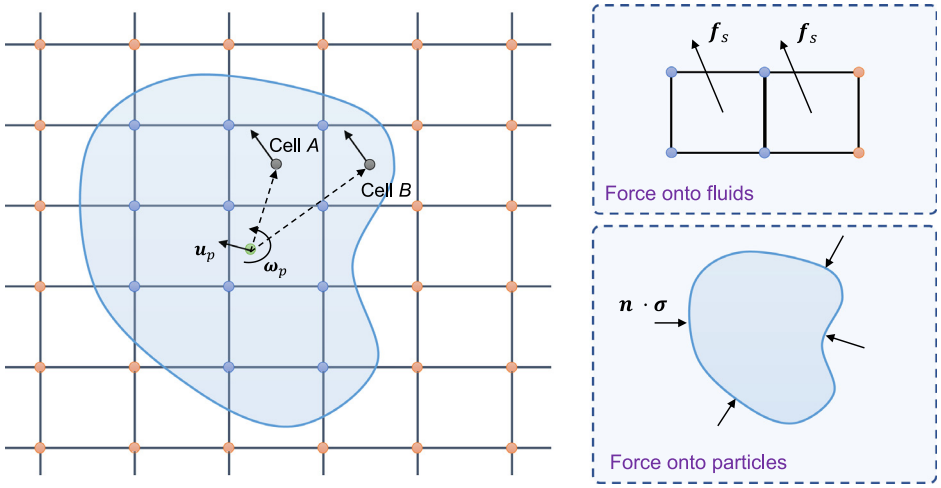

Fig. 2. Illustration of the IBM approach for fluid–particle interaction.

where $\boldsymbol{x}_i$ is the mesh cell center, $\boldsymbol{x}_p$ is the particle centroid, and $\boldsymbol{u}_p$ and $\boldsymbol{\omega}_p$ are the particle velocity and spin, respectively. Thereby, the IBM-related source force $\boldsymbol{f}_{IB}$ is calculated as

$$\boldsymbol{f}_{IB} = (\hat{\boldsymbol{u}}_f - \boldsymbol{u}_f)/A_u \tag{21}$$

where A_u is a coefficient derived from the momentum Eq. (2). Specifically, in reference to *OpenFOAM* library, the left hand side of Eq. (2) can be split into $A_u\boldsymbol{u} + H$, where $A_u\boldsymbol{u}$ and H represent the implicit and explicit parts of the momentum, respectively [32].

The force applied onto particles by the fluids is integrated from the fluid forces that acts on the surfaces of a particle [61], which, after applying the divergence theorem, is calculated as

$$\boldsymbol{F}_f = \sum^{cells} (\varphi_s \nabla \cdot \boldsymbol{\sigma} - (1-\varphi_s)\boldsymbol{f}_{IB})\, V_c \tag{22}$$

$$\boldsymbol{M}_f = \sum^{cells} (\boldsymbol{x}_i - \boldsymbol{x}_p) \times (\varphi_s \nabla \cdot \boldsymbol{\sigma} - (1-\varphi_s)\boldsymbol{f}_{IB})\, V_c \tag{23}$$

where $\sum^{cells}$ indicates the summation over all cells that are overlapped by a particle, and V_c is the cell volume. Herein, the term $(1-\varphi_s)\boldsymbol{f}_{IB}$ accounts for the errors due to the averaging effects of fluid and solid velocities at the partially overlapped cells, where the derivation is presented in the following.

In addition to the volume fraction-based IBM used in this work, there is another type of IBM which is based on boundary points (also termed Lagrangian points) [61,62]. Both types of IBM have their advantages and drawbacks. In the case of boundary-point based IBM, the particle–fluid interface is represented by discrete boundary points, which are used to transfer information (e.g., velocity and force) between fluids and particles. The boundary points-based IBM could therefore better achieve the no-slip boundary condition required at the particle–fluid interface, whereas the volume fraction-based IBM cannot accurately account for the interface (but the center of fluid cells) unless the mesh is sufficiently fine. It is worth noting that the SDF-DEM is also adaptable and beneficial to the boundary points-based IBM. In SDF-DEM, particles are discretized with surface points for contact detection and resolution, where these surface points could be conveniently used by the boundary points-based IBM for particle–fluid interaction. The SDF-DEM is equipped with a particle surface discretization method based on weighted spherical centroidal Voronoi tessellation [50], which has the advantage of obtaining any number of surface points with uniform spatial distribution. This feature is important to the accuracy of the boundary points-based IBM, especially for irregular-shaped particles.

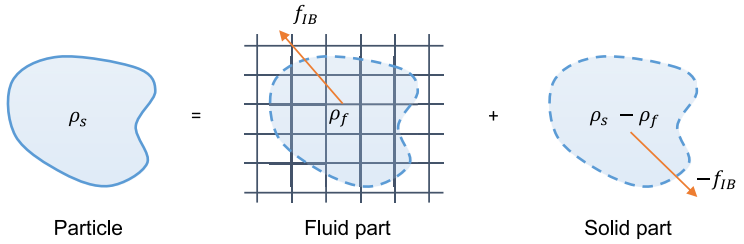

Fig. 3. Illustration of dividing a particle into two fictitious parts for deriving the fluid–particle interaction force based on the IBM.

2.4. Derivation of corrected IBM force

Considering a particle with density ρ_s, it can be regarded as a combination of two parts, namely fluid part with density ρ_f and solid part with density $\rho_s - \rho_f$ (see Fig. 3). The fluid part and solid part are connected with fictitious springs, which results in the IBM-related source force (i.e., f_{IB} in Eq. (2)). The motion of the fluid part is characterized by the Navier–Stokes equation, and integrating the momentum equation over the domain overlapped by the particle gives

$$\sum^{cells}\left(\rho_f\frac{\partial \boldsymbol{u}_f}{\partial t}+\nabla\cdot(\rho_f\boldsymbol{u}_f\otimes\boldsymbol{u}_f)\right)\varphi_s V_c=\sum^{cells}\left(\nabla\cdot\boldsymbol{\sigma}+\rho_f\boldsymbol{g}+\boldsymbol{f}_{IB}\right)\varphi_s V_c \tag{24}$$

where $\boldsymbol{\sigma}=-\nabla p+\nabla\cdot(\mu_f\nabla\otimes\boldsymbol{u}_f)$ is the fluid stress, and the surface tension is neglected for simplicity. Substituting the left hand side with the average fluid acceleration $\boldsymbol{a}$ in the material configuration, Eq. (24) can be written as

$$\rho_f V_p\boldsymbol{a}=\sum^{cells}\left(\nabla\cdot\boldsymbol{\sigma}+\boldsymbol{f}_{IB}\right)\varphi_s V_c+\rho_f V_p\boldsymbol{g} \tag{25}$$

where V_p is particle volume, and the averaged fluid acceleration $\boldsymbol{a}$ is close to particle acceleration $\boldsymbol{a}_p$ due to the constraint of rigid motion from particle. Following the strategy in [60], the averaged fluid acceleration $\boldsymbol{a}$ could be decomposed into $\boldsymbol{a}=\boldsymbol{a}_p+\boldsymbol{a}_r$, where $\boldsymbol{a}_r\approx\boldsymbol{0}$ represents the errors due to mesh resolution and the fact that fluid motion is not rigid. For the solid part, the motion is governed by the Newton's equation written as

$$(\rho_s-\rho_f)V_p\boldsymbol{a}_p=(\rho_s-\rho_f)V_p\boldsymbol{g}-\sum^{cells}\boldsymbol{f}_{IB}V_c \tag{26}$$

Adding up Eqs. (25) and (26), and substituting $\boldsymbol{a}$ with $\boldsymbol{a}_p+\boldsymbol{a}_r$ would give

$$\rho_s\boldsymbol{a}_p+\rho_f V_p\boldsymbol{a}_r=\rho_s V_p\boldsymbol{g}+\sum^{cells}\left(\nabla\cdot\boldsymbol{\sigma}+\boldsymbol{f}_{IB}\right)\varphi_s V_c-\sum^{cells}\boldsymbol{f}_{IB}V_c \tag{27}$$

Thereby, the force applied on particle by fluid is calculated as

$$\boldsymbol{F}_f=\sum^{cells}\left(\varphi_s\nabla\cdot\boldsymbol{\sigma}-(1-\varphi_s)\boldsymbol{f}_{IB}\right)V_c \tag{28}$$

It should be noted that the surface tension at the interface of solid and multiphase fluids is not rigorously considered in the present SDF-CFD-DEM formulation, which may result in certain errors in cases (e.g., contact angle, liquid bridge) when surface tension effect is important. Eq. (28) contains an IBM related term $(1-\varphi_s)\boldsymbol{f}_{IB}$, comparing with convectional formulation of fluid force onto particles [31,44,47]. This term vanishes with the increase of mesh resolution. The strategy of dividing a particle into two fictitious parts does not require a specific combination of densities, which results in two options commonly used in the literature, namely with and without correcting the fluid density to particle density for cells overlapped by a particle [63,64]. According to our simulations, the former option (i.e., with density correction) exhibits better accuracy in capturing the interface of multiphase fluids (e.g., water and air) with distinct fluid densities.

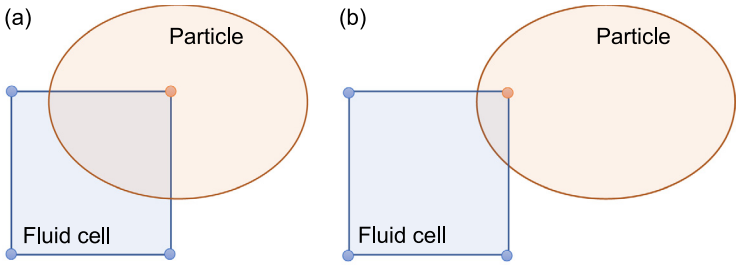

Fig. 4. Illustration of the calculation of solid volume fraction for a fluid cell.

2.5. SDF-based estimation of solid fraction

In the IBM approach, a key step is to find the solid volume fraction of the fluid cells that are overlapped by particles. A most straightforward approach is to first construct a high-resolution surface of the particles and then compute the volume fraction based on the mesh Boolean intersections of the fluid cells and particles. This approach, however, is fairly computationally expensive due to the computation of mesh Boolean intersection. Another simple approach is to count the number of cell nodes that are inside and outside of the particles [65]. The node-based approach estimates the solid fraction as

$$\phi_s = \frac{N_{vc} + N_{cc} N_v}{2N_v} \tag{29}$$

where N_v is the number of vertices in a cell, and N_{vc} and N_{cc} are the number of vertices and centers intersecting the particle, respectively. The node-based approach can only provide a discrete varying solid fraction and may result in considerable errors in the solid fraction, as depicted in Fig. 4. Following a strategy similar to the node-based approach, this work introduces a SDF-based approach by utilizing the SDF values of each cell node. The SDF-based approach estimates the solid fraction as

$$\phi_s = \frac{\sum^{N_{vc}} \Phi_{v,i}}{\sum^{N_v} |\Phi_{v,i}|} \tag{30}$$

where $\sum^{N_{vc}} \Phi_{v,i}$ represents the summation of the SDF values of the cell nodes inside particles and $\sum^{N_v} |\Phi_{v,i}|$ represents the summation of the absolute SDF values of all cell nodes.

As potential future extensions, the SDF could also facilitate the calculation of wall distances for turbulence modeling [66,67] and the calculation of curvature and surface normal at particle–fluid interface for surface tension modeling [68]. In addition, in the IBM-based coupled CFD-DEM, a challenging and computationally intensive part is to map the particles to the fluid mesh (i.e., to classify the mesh cells and nodes that are occupied by the particles). With the SDF representation of particles, the classification of mesh cells and nodes can be handled efficiently and robustly by simply testing the signs of each mesh node, without the need of conventional mesh intersection tests. Numerical aspects and implementation of the SDF-CFD-DEM are presented in the subsequent section.

3. Numerical aspects and implementation

3.1. Searching for solid nodes

In the resolved CFD-DEM, there are frequent needs to query the fluid cells overlapped by a particle, e.g., for calculating solid volume fraction. To improve the computational efficiency, a linked list that maps CFD mesh nodes to DEM particles is introduced and implemented in the CFD-DEM coupler. The linked list functions as that given a query node, it returns all the particles that overlap this node. By the virtue of SDF-based particle description, the nodes-to-particles linked list can be efficiently constructed by testing the sign of the SDF at a given node with respect to each particle. Nonetheless, the construction of nodes-to-particles linked list for each node still has a time complexity of $O(N)$ in a brute-force manner, where N is the number of all particles. For computational efficiency, the cell-based searching algorithm for broad-phase contact detection in DEM is further unitized. As illustrated in

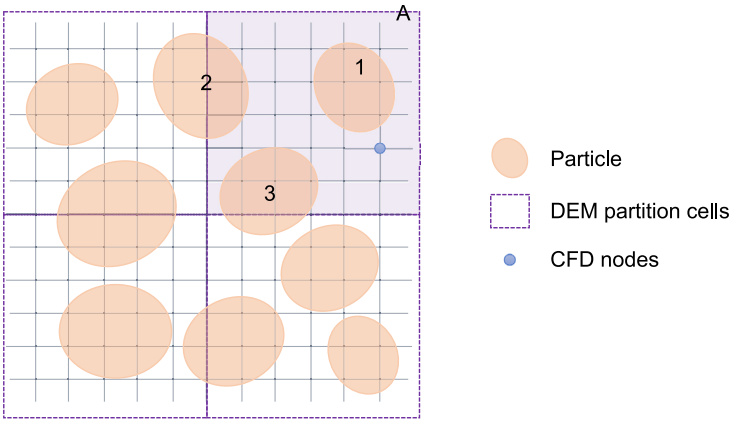

Fig. 5. Illustration of the cell-based node searching algorithm.

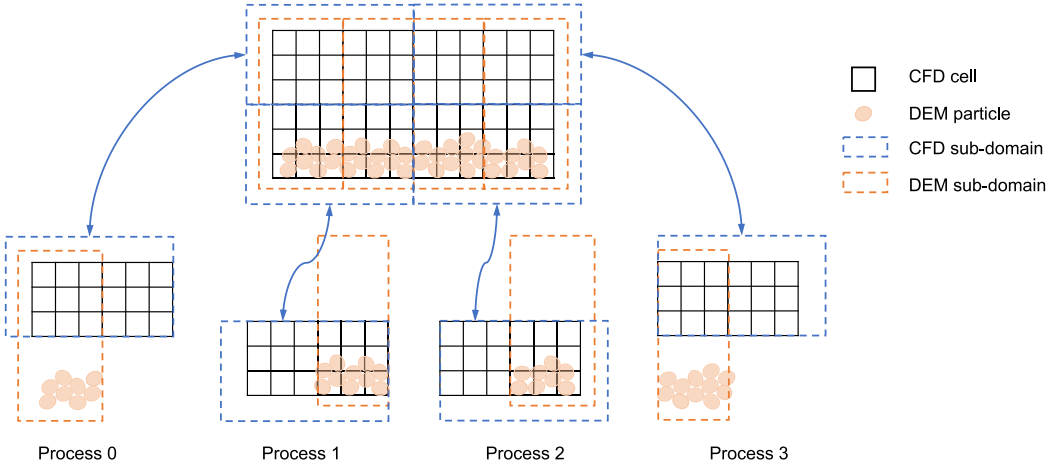

Fig. 6. Illustration of the domain discretization schemes in CFD and DEM.

Fig. 5, the cell-based approach partitions the DEM domain into a set of cells, with each cell being linked to the particles that overlap this cell. For a certain CFD node, to construct its linked particles, the DEM partition cell that encloses this node is first obtained. Then, the particles that are linked to this partition cell are queried to determine the particles that enclose the given CFD node. For example, a given CFD node is enclosed by DEM partition cell *A*, and thus only the particle 1, 2, and 3 that are linked with partition cell *A* are tested for construing the node-to-particles list for this CFD node.

3.2. Domain discretization

Both the CFD (by leveraging *OpenFOAM*) and the SDF-DEM code support parallel computing via Message Passing Interface (MPI). Simulation data is distributed among different processors and there is a need of data exchange between processors. Due to the different distribution of fluids and particles, the CFD domain and DEM domain generally require different schemes to optimize the load balance among different processors. As illustrated in Fig. 6 in two-dimension, for an example parallel simulation with 4 processors, the CFD domain is discretized into 2 by 2 sub-domains, whereas the DEM domain is discretized into 4 by 1 sub-domains as the particles are mostly scattered at the lower part of the whole domain. To compute fluid–particle interaction, the particle data in Processor 0 and 3 should be synchronized to Processor 1 and 2, respectively. For simplicity, in this work the DEM data of each processor is synchronized to all other processors in each CFD-DEM coupling cycle. The MPI-based algorithms for DEM data synchronization are implemented.

3.3. Timestep and synchronization

For the FVM-based CFD, the Courant number should be generally smaller than 1.0 to ensure numerical stability and simulation accuracy. The Courant number C_o is defined as

$$C_o = 0.5\frac{\phi}{V_c}\Delta t_{CFD} < 1.0 \tag{31}$$

where ϕ is the fluid flux of a fluid cell. For DEM, the critical timestep could be estimated as

$$\Delta t_{DEM,critical} = \sqrt{m/k_n} \tag{32}$$

where m is particle mass and k_n is the contact normal stiffness. In CFD-DEM simulations, the timestep Δt_{DEM} of DEM is usually much smaller than the timestep Δt_{CFD} of CFD. An inner loop of DEM is implemented to synchronize the mechanical time between CFD and DEM.

3.4. Solution procedures

For the implementation of the resolved SDF-CFD-DEM, the open-source library *OpenFOAM* is used for CFD, whereas the in-house SDF-DEM code is adopted for the DEM [50]. New resolved CFD-DEM coupler is implemented under the SDF framework. The CFD and DEM are solved respectively, with the exchange of particle–fluid interaction forces. The simulation data can be dumped as *OpenFOAM* files for CFD and *VTK* files for DEM, both of which can be conveniently visualized in *ParaView*. As illustrated in Fig. 7, the major solution procedures of the resolved SDF-CFD-DEM are summarized as follows:

1. Initialize CFD with the domain geometry, domain and mesh discretization, velocity field, pressure field, and boundary conditions.
2. Initialize DEM with particles, boundary walls, contact models and domain discretization.
3. For the case of parallel computing, synchronize the particle data such as geometry, position and velocity to all processors.
4. Update the linked list that maps particles to CFD mesh nodes.
5. Update the solid fraction field using Eq. (30) and correct the fluid density field.
6. Calculate the fluid force acting on the particles via Eqs. (22) and (23).
7. Run DEM for time Δt_{CFD} through an inner loop with steps (1) contact detection and resolution, (2) evaluation of contact forces, (3) computation of particle motion and (4) updating of particle geometric descriptions.
8. Solve the continuity equation, update the VOFs of fluids, and reconstruct the phase interface using the isoAdvector scheme.
9. Update the Navier–Stokes momentum equation and solve for a prediction of the velocity using data (e.g., velocity and pressure field) from previous time step.
10. Calculate the IBM-related source force via Eq. (21) to account for the influence of particle motion on fluids. Repeat this step following the pressure implicit with splitting of operators (PISO) scheme [69] with the prescribed number of iterations.
11. Go to step (3) to repeat the entire CFD-DEM simulation until reaching the end time.

4. Verification tests

In this section, the accuracy of the SDF-based solid fraction is first investigated by comparing with the traditional node-based approach, as well as the mesh-Boolean-based analytic solution. Particle settling test and drafting–kissing–tumbling test are then presented to verify the applicability and accuracy of the proposed SDF-CFD-DEM, with benchmark results from the literature.

4.1. Results of solid fraction

To verify the proposed SDF-based approach for calculating solid fraction field, CFD-DEM models with different types of particles are created, including sphere, ellipsoid, poly-super-quadrics, spherical harmonics, polyhedron and level set. Each type of particle has its own formulation of particle shape and thus implements different functions of

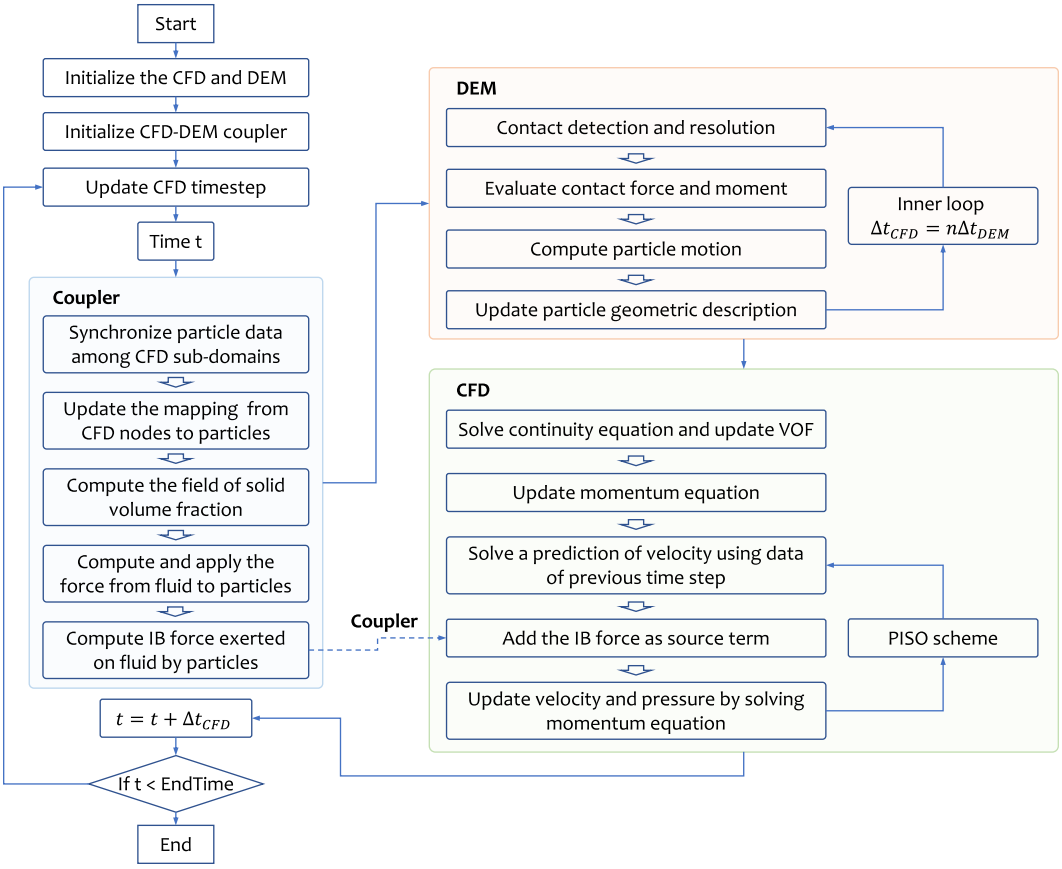

Fig. 7. Flow chart of the resolved multiphase CFD-DEM.

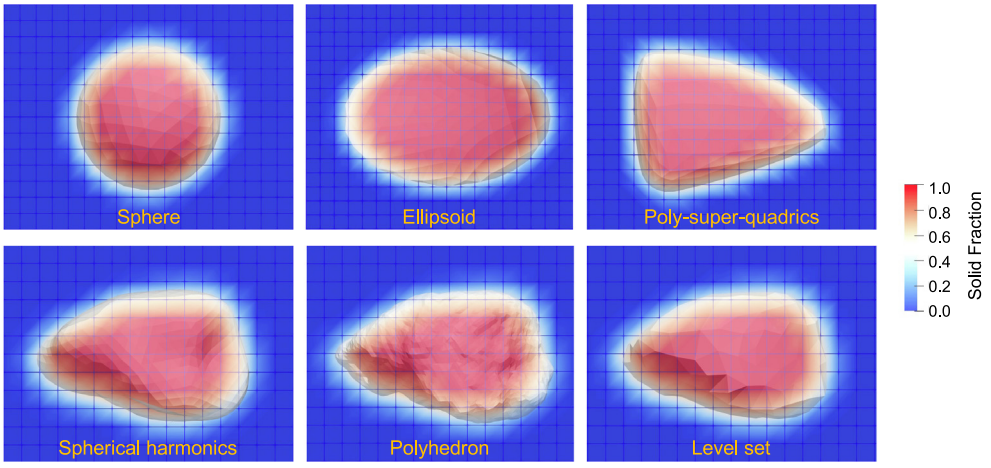

Fig. 8. Examples of SDF-based estimation of solid fraction field for different types of particles.

SDF [50]. Fig. 8 shows the calculated solid fraction fields, where the CFD cell size is about 1/10 of the equivalent particle size. The profiles of non-zero solid fraction cells match well with the surfaces of particles.

As a quantitative investigation, the solid fraction at the cells that are partially overlapped by a particle is extracted and compared with the benchmark values. Herein, the benchmark solid fraction is calculated using the mesh

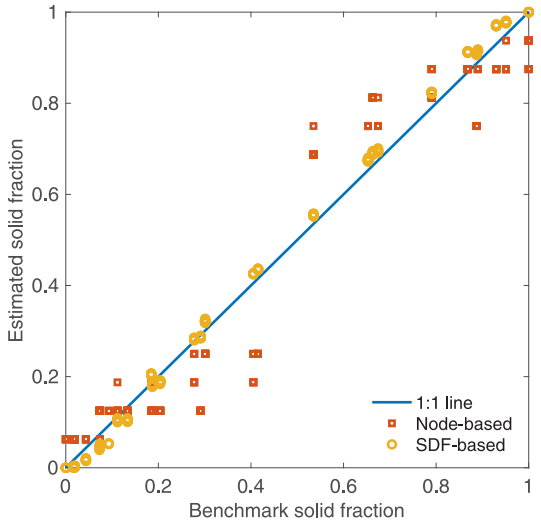

Fig. 9. Errors in the estimated solid fraction of the node-based and SDF-based approaches.

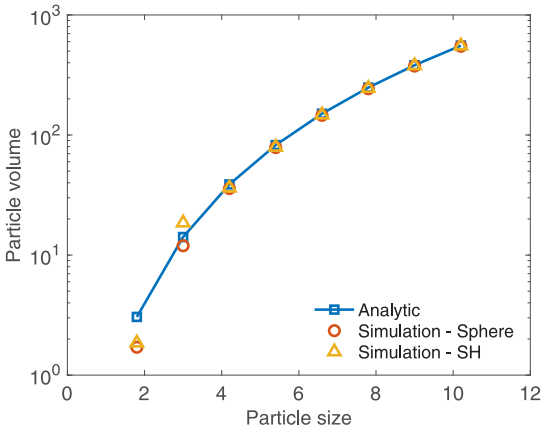

Fig. 10. Particle volume calculated based on the solid fraction of fluid field. Particle size is normalized by the size of fluid cell. SH represents a spherical harmonics particle shown in Fig. 8.

intersection approach. In addition, the node-based approach is also implemented and adopted as a comparison. Fig. 9 plots the estimated solid fraction of the node-based approach and the SDF-based approach, respectively. The results of the SDF-based approach scatter closely to the 1:1 line, indicating the considerably good accuracy of the SDF-based approach. In addition, the SDF-based approach exhibits notably better accuracy than the node-based approach. It is worth noting that the comparison are performed considering various random positions of particles on the fluid mesh, thereby avoiding the mesh and sampling dependency to a great extent.

The solid fraction field represents a projection of the particles onto the fluid mesh, where the accuracy could be also affected by the mesh resolution. To investigate this aspect, the volume of a particle is calculated by integrating the solid fraction over the CFD mesh and is compared with the analytic solution. Fig. 10 plots the results of particle volume for the cases of different particle sizes. It could be observed that for particles with size less than 4 times of CFD cell size, there is noticeable errors in the particle volume evaluated based on the solid fraction. The error vanishes with increasing particle size (or increasing CFD mesh resolution).

Table 1
Specifications and results of the settling tests of spherical particles, where v_∞ indicates the eventual steady-state settling velocity. The laboratory experiment results are obtained from ten Cate et al. [70].

Case number	ρ_f [kg/m^3]	μ_f [$\times 10^{-3}$ Ns/m^2]	v_∞, exp. [m/s]	Re [-]	v_∞, sim. [m/s]
Case 1	970	373	0.038	1.5	0.037
Case 2	965	212	0.060	4.1	0.059
Case 3	962	113	0.091	11.6	0.089
Case 4	960	58	0.128	31.9	0.122

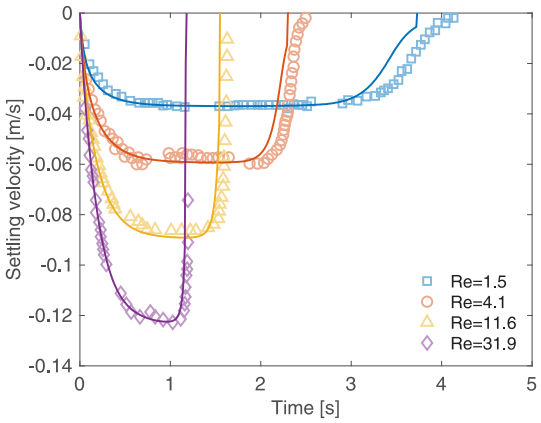

Fig. 11. Evolution of settling velocity of spherical particles for the cases of different fluid densities and viscosity. The markers indicate the results of laboratory experiments from ten Cate et al. [70], and the lines represent the results of SDF-CFD-DEM simulations.

4.2. Settling of single particle

In this test, a particle is initially placed in a fluid before being released to settle down under gravity. The particle will eventually reach a steady settling velocity, which is a function of the fluid and particle properties (e.g., fluid density, viscosity, particle shape, etc.). Results of particle setting tests could be used to derive formulations of drag coefficient, which has wide applications in various disciplines.

4.2.1. Spherical case

For spherical particle case, the laboratory experiment results previously reported in ten Cate et al. [70] are adopted as the benchmark results for the verification. The particle has a diameter of 0.015 m and a density of 1120 kg/m^3. The container has a base of 0.01 m by 0.01 m, and the particle is initially hanging 0.012 m from the bottom of the container. The specification of the fluids are listed in Table 1, with different values of fluid density and viscosity. In the simulation, the CFD mesh size is taken 1/12 of particle size. The timestep is specified as 1.0×10^{-3} s for the CFD and 1.0×10^{-7} s for the DEM. Fig. 11 plots the evolution of particle settling velocity with time for the cases of different fluids, and the eventual steady-state settling velocities are summarized in Table 1. All results of SDF-CFD-DEM simulations are in good agreement with those of laboratory experiments.

To gain insights into the effect of mesh size on the accuracy of the volume fraction-based IBM, a series of particle settling tests are performed with particle size to mesh size ratio ranging from 3 to 18. Fig. 12 shows the evolution of settling velocity for the cases of different ratios of particle size to mesh size. For a size ratio smaller than 6, the particle–fluid interaction force would be significantly underestimated, resulting in a notable increase in the terminal settling velocity. The error in the terminal settling velocity becomes less than about 10% when the size ratio gets greater than 9, and it gradually converges when the particle size to mesh size ratio reaches 15 or higher. It is speculated that for the cases of coarse meshes, the numerical errors may originate from two possible sources. The first is that the no-slip boundary condition required at the particle–fluid interface is difficult to achieve with the volume fraction-based approach currently employed. The second is the volume integration based on discretized cells and estimated solid fraction. We have probed the value of particle weight (the gravity term in the Navier–Stokes

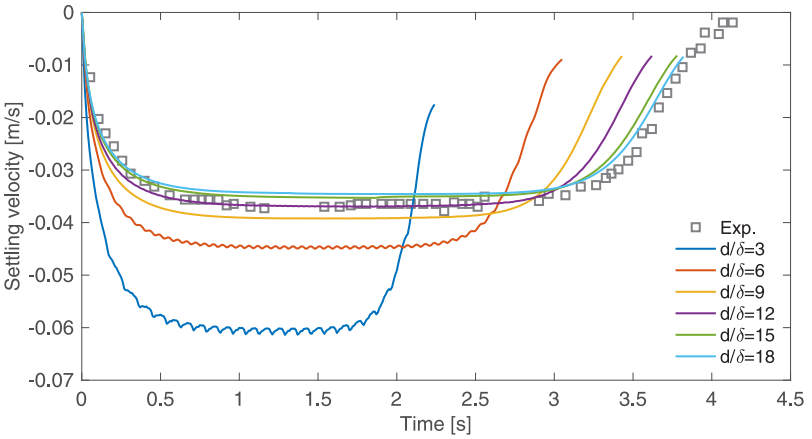

Fig. 12. Evolution of settling velocity of spherical particles for the cases of different particle size (d) to mesh size ratios (δ).

equation) based on volume integration and found it to be slightly smaller than the analytical value. Thereby, we conjecture that the hydrodynamic force based on volume integration would also be underestimated in this example case. Both types of errors could be mitigated by increasing the fluid mesh resolution. According to the results of mesh sensitivity study, the ratio of particle size to mesh size should be greater than 15 for high-resolution fluid–particle interactions, and a value around 10 is desirable for granular flow involving many particles for the sake of computational efficiency.

4.2.2. Irregular-shaped case

For irregular-shaped particle case, the laboratory experiments recently reported in Fan et al. [71] are adopted for the verification. In their experiments, particles of a series of elongation, flatness and blockiness are created based on super-ellipsoid and three-dimensional printing. The surface function of a super-ellipsoid particle is given as

$$\left|\frac{x}{a}\right|^{2/\epsilon} + \left|\frac{y}{b}\right|^{2/\epsilon} + \left|\frac{z}{c}\right|^{2/\epsilon} = 1 \tag{33}$$

where a, b, and c are the semi-major lengths along the principal axes x, y, and z, respectively, and ϵ is a shape parameter that controls the blockiness of the particle shape. For ellipsoid particles, the elongation index EI and flatness index FI are calculated as $EI = b/a$ and $FI = c/b$, respectively. In this work, simulations of five particles with $\epsilon = 2$, $EI = 1$, and $FI = 0.2,\ 0.4,\ 0.6,\ 0.8,\ 1.0$, are conducted, respectively. All particles have the same equivalent size of 9.85 mm and the particle density is 1200 kg/m^3. For the fluid, the density is 1120 kg/m^3 and the viscosity is 7.47×10^{-3} Ns/m^2. Fig. 13 presents the evolution of settling velocity of the five particles with different flatness. It is clearly observed that the steady-state settling velocity decreases notably with the increase of flatness (i.e., decreasing FI value). The comparison of the stead-state settling velocity between laboratory experiments and SDF-CFD-DEM simulations are presented in Fig. 14, where the simulation results are in good agreements with the results of laboratory experiments.

4.3. Drafting–kissing–tumbling of two particles

For the volume fraction-based IBM, the coupling is applied at the center of fluid cells, thus it may not accurately reflect the situation of different particle surface velocities and achieve the no-slip boundary condition required at particle–fluid interface, considering the case of two adjacent particles. In addition, in the current formulation and implementation of the volume fraction-based IBM, the solid fraction accounts for the contribution of both particles, and the solid velocity is taken as the average of the surface velocities of the two particles. This could lead to another potential source of error in fluid–particle interaction. To address this concern, a simulation of the drafting–kissing–tumbling test involving two particle interactions is conducted.

In the drafting–kissing–tumbling test, two particles are placed within a fluid with a small distance in the z direction. After releasing, the two particles would subsequently exhibit drifting, kissing and tumbling behaviors

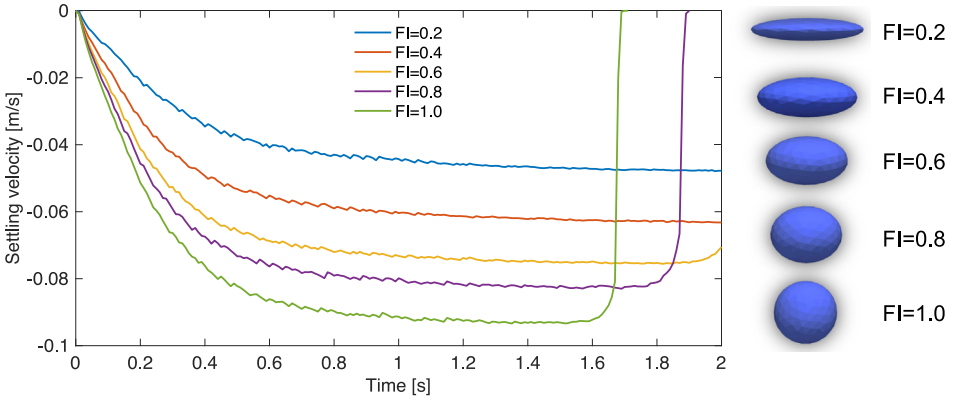

Fig. 13. Evolution of settling velocity of ellipsoid particles with different flatness based on SDF-CFD-DEM simulations.

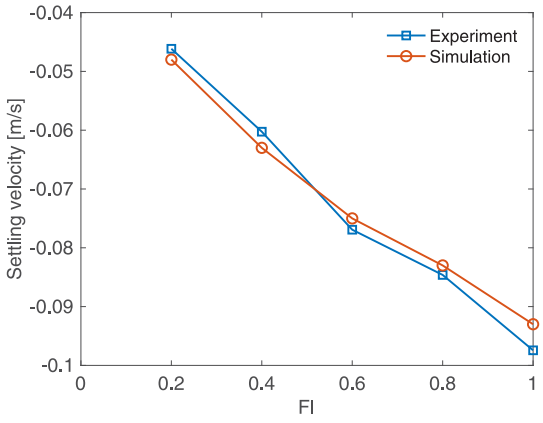

Fig. 14. Comparison of the stead-state settling velocity between laboratory experiments [71] and present SDF-CFD-DEM simulations.

during the settling process, which has been well observed in both laboratory experiments and numerical simulations [62,72–74]. Fig. 15 illustrates the setup of the drafting–kissing–tumbling simulation. Both particles have a diameter of 0.167 cm and their initial separation distance is 0.34 cm. The fluid domain is of 1.0 cm by 1.0 cm by 4.0 cm and is discretized into 50 by 50 by 200 cells. The fluid is assumed to be water with a density 1000 kg/m^3 and a viscosity 0.001 Ns/m^2. For the DEM, a linear contact model is adopted with normal stiffness 2.0×10^6 N/m, shear stiffness 1.0×10^6 N/m, and zero contact friction and damping. The CFD is specified with adaptive timestep, whereas the DEM has a timestep of 1.0×10^{-7} s. As shown in Fig. 15, the trailing particle first exhibits a drafting behavior at the beginning 0.34 s and then hits the leading particle; finally, the leading and trailing particles switch their leading and trailing roles as a tumbling behavior. The evolution of settling velocities of the two particles with time are plotted in Fig. 16. The result of the present SDF-CFD-DEM simulation matches well with that in a previous study [62]. There is a minor discrepancy in the settling velocity at the time when the two particles approach and collide with each other, which may be due to the above-mentioned potential errors of the volume fraction-based IBM.

5. Illustrative examples

This section presents four illustrative examples to further showcase the capability of the developed SDF-CFD-DEM. The examples include collision of irregular-shaped particles, water entry of various types of particles, immersed granular collapse, and mudflow and bedload transport, which involve complex interactions between multiphase fluid and irregular-shaped particles.

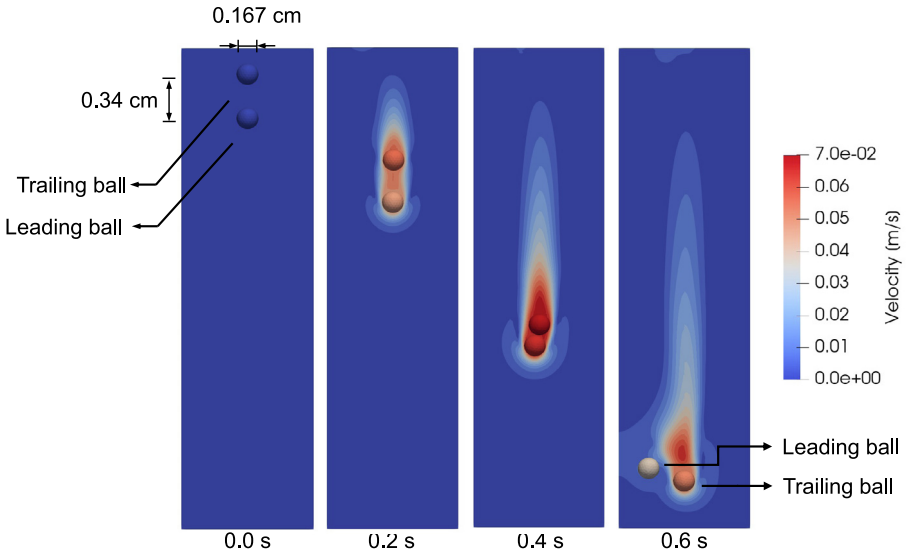

Fig. 15. Simulation setup and snapshots of the drafting–kissing–tumbling test of two spherical particle.

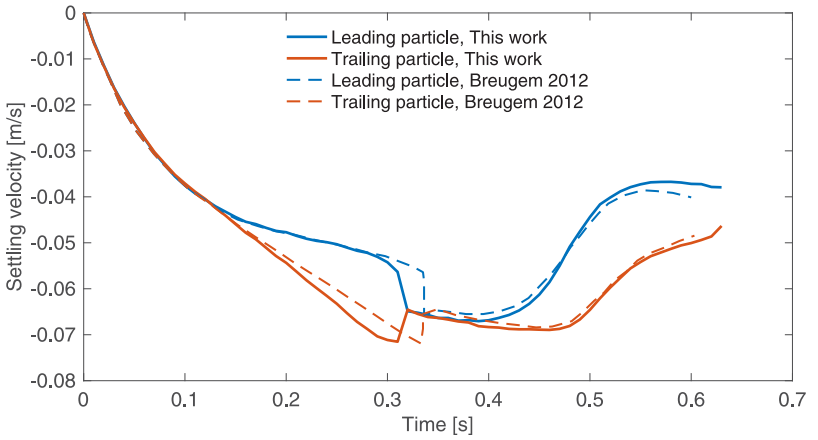

Fig. 16. Evolution of settling velocity of the two spherical particles in the drafting–kissing–tumbling test.

5.1. Collision of irregular-shaped particles

In the proposed SDF-CFD-DEM, the contact potential based energy conservative contact theory is adopted to resolve the contact behavior between arbitrary-shaped particles. The energy conservation characteristics enables quantitative energy analysis of a CFD-DEM simulation, making it another attractive feature of the SDF-CFD-DEM. For the first example, the collision between two immersed particles is considered, where the energy evolution during colliding process is studied. In this example, two particles are placed in a free water stream with an initial separation distance of 0.01 m. One particle is fixed and another particle is specified with an initial velocity of 0.02 m/s approaching towards the former particle, which would result in a collision after about 0.5 s. Both particles have an equivalent diameter of 0.02 m and a density of 7,800 kg/m^3. The linear contact model is adopted with normal stiffness 2.0×10^6 N/m, shear stiffness 1.0×10^6 N/m, and the contact friction and contact damping are both zeros. The gravity is not considered in this example to facilitate the investigation of the kinetic energy evolution. Fig. 17 shows several snapshots of particle collision example, where two cases are considered, namely an irregular-shaped particle case and a spherical case. The effect of particle shape irregularity on the potential vortexes in the fluid can be clearly observed, by comparing the fluid velocity fields of the two cases.

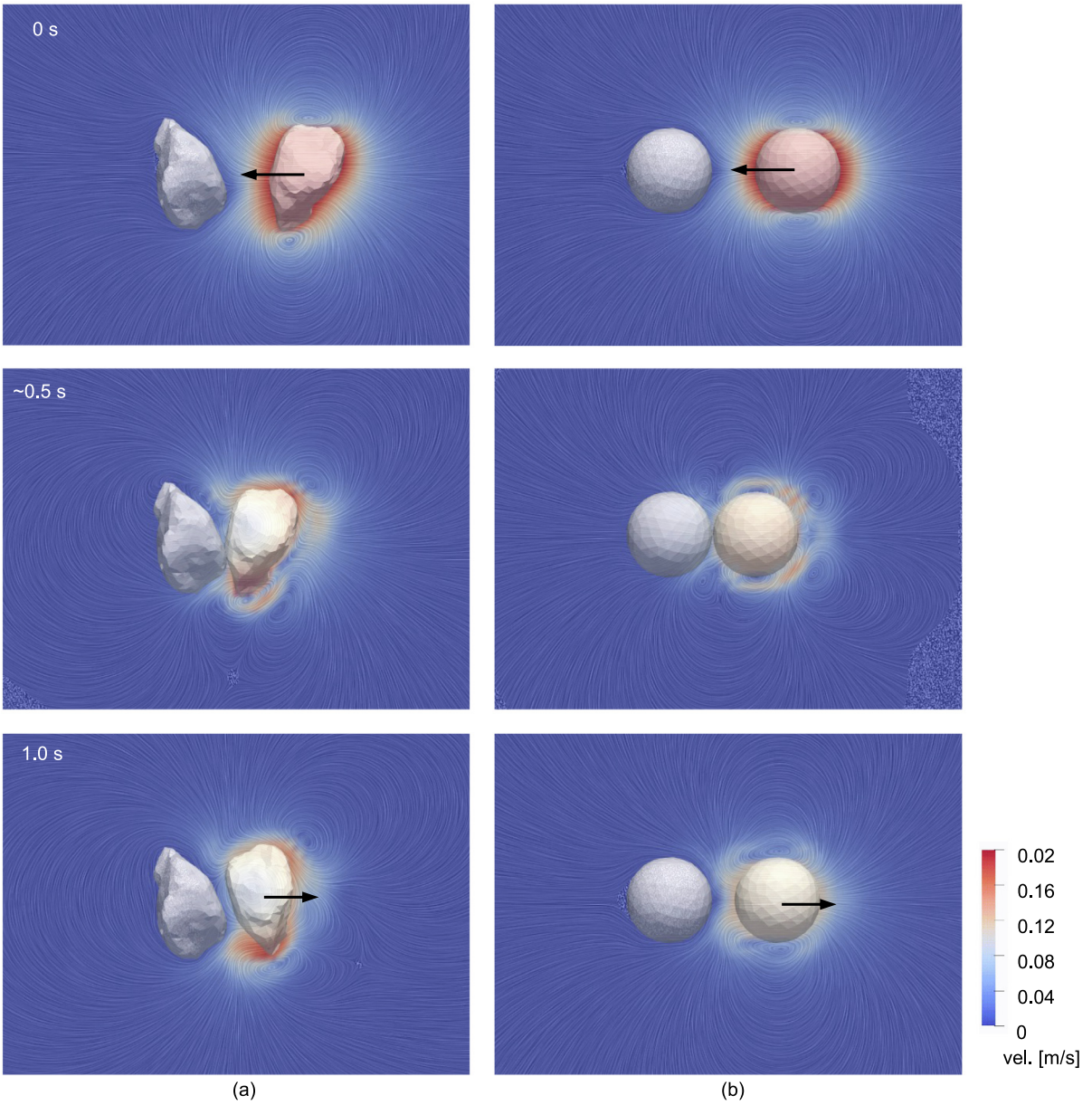

Fig. 17. Snapshots of the collision tests on (a) irregular-shaped particles and (b) spherical particles. The fluid field is rendered using *Surface LIC* (line integral convolution) in *ParaView*.

The evolution of particle approaching velocity and kinetic energy are plotted in Fig. 18. For the case of dry collision between two irregular particles, the particle translation velocity decreases after the collision, as some of the translational energy is converted to the rotational energy. Nonetheless, the particle kinetic energy keeps constant during the whole simulation, indicating the good accuracy of the contact resolution algorithm. For the immersed cases, particles would first experience a slight decrease in the translational velocity; and after collision, the particle translational velocity decreases notably due to the fluid viscosity effect [75,76]. The viscous damping effect is more notable in the irregular-shaped particle case than in the spherical particle case, as the irregular-shaped particle has a larger cross section perpendicular to the particle moving direction in this case. The results demonstrate the good capability of the SDF-CFD-DEM to capture the energy evolution characteristics of arbitrary-shaped particles.

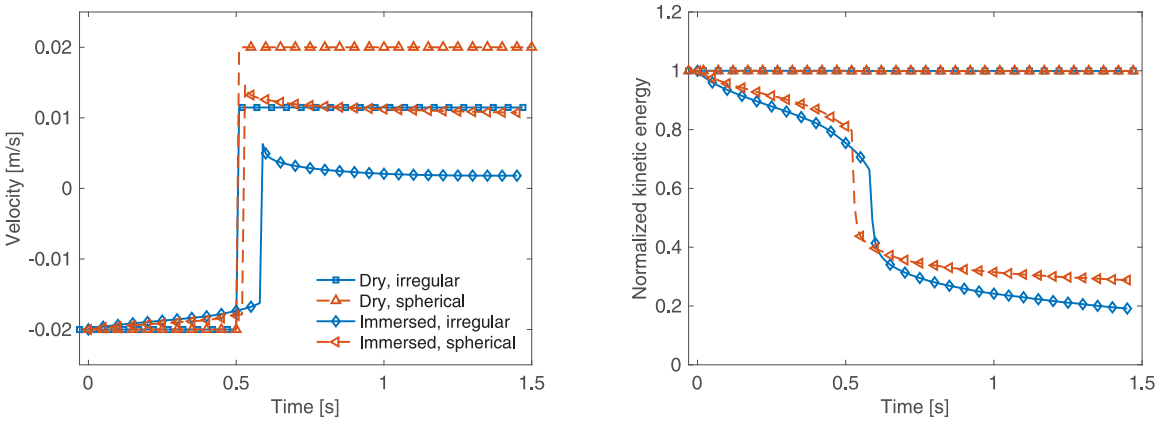

(a) (b)

Fig. 18. Evolution of (a) x-component of particle translational velocity and (b) particle kinetic energy (normalized by the initial particle kinetic energy).

5.2. Water entry of various types of particles

In the water entry example, a number of particles are inserted into the top part of a cubic box container of dimension 1.0 m. The particles are allowed to enter the water and settle down under gravity. Cases of different particle models, including poly-super-quadrics, spherical harmonics, polyhedron, level set as showcased in Fig. 8, are considered. In all cases, the particles are assumed to have an equivalent size of 0.1 m and density 2650 kg/m^3. The linear contact model is adopted with normal stiffness 2.0×10^6 N/m, shear stiffness 1.0×10^6 N/m, contact friction 0.5; and, the contact damping coefficient is 0.7. The water depth is 0.5 m, and the whole fluid domain is discretized into 100 by 100 by 100 cells. Fig. 19 shows some snapshots of the water entry example, including the particle positions, water-air interface, and the 0.5 isosurface of solid fraction field. There are two worthwhile noting observations. First, the 0.5 isosurfaces of solid fraction field match well with the surfaces of particles, indicating the good accuracy of the SDF-based approach for estimating solid fraction. Second, with the entering of particles into the water, the water-air interface are pushed inwards into the water. It would then result in bubbles when the water-air interfaces close up. In addition, eventually when the particles settles, the air phase initially overlapped by the particles would remain inside the particles. The mass of water and air is conserved, leading to an level-up in the water surface. Fig. 20 shows the velocity contours and streamlines during the particle settling process. At the very beginning of the entering and settling process, there are vortices that could be observed near particles; the fluid velocity field and streamlines become rather chaotic after the particles settle down. The results demonstrate the good capability of the SDF-CFD-DEM approach for modeling irregular-shaped particle dynamics.

5.3. Immersed granular collapse

In this example, immersed granular collapse tests on bulk irregular-shaped particles under water are conducted to investigate the effect of particle shape and ambient fluid on the forming of sandpile. As illustrated in Fig. 21, the column consists of 320 irregular-shaped particles of equivalent diameter of 3.86 cm and has a dimension of about 20 cm (width) by 20 cm (depth) by 50 cm (height). The particles are modeled by spherical harmonics based on the SDF-DEM approach. With the column of irregular-shaped particles, collapse is proceeded by removing the left wall that confines the particles. The model parameters for the numerical simulation are summarized in Table 2. As a comparison, the column collapse test on spherical particles is also conducted. This test also involves two phases of fluids to demonstrate the performance of the SDF-CFD-DEM in modeling free surface and its interaction with particles.

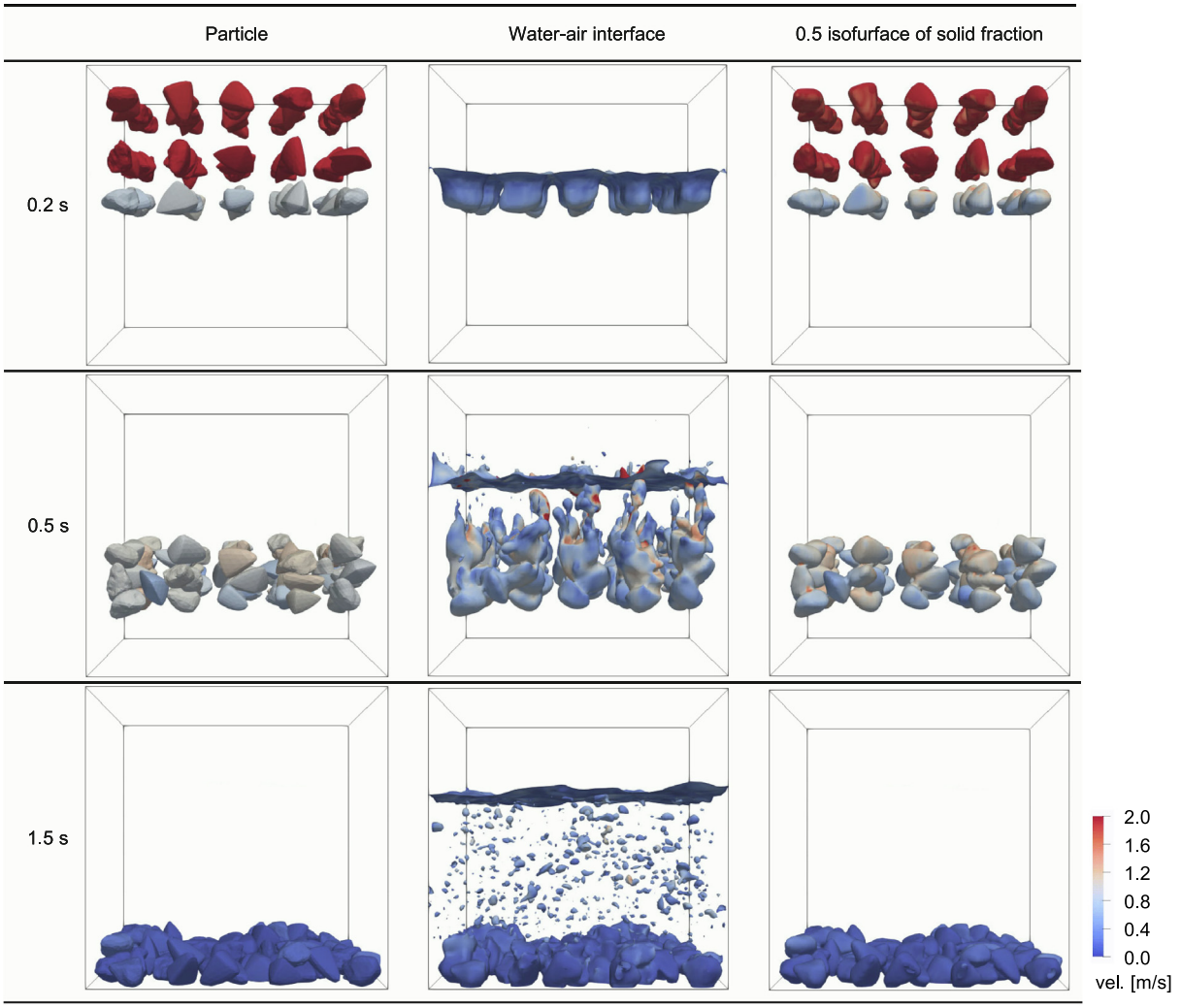

Fig. 19. Snapshots of the particle, water-air interface, and 0.5 isosurface of solid fraction filed for the example of water entry and settling of various types of particles. The color represents velocity interpolated from the fluid velocity field.

Snapshots of the column collapse under different water conditions are gathered in Fig. 22. At the beginning 0.3 s, the fluid is pushed away, resulting in a small cavity of air at the front of particles. Particles transfer their kinetic energy to the fluid by driving the fluid to move with the particles at this stage. Then, at around 0.5 s, the fluid floods back toward the particles due to the existence of cavity and thus counteracts the left moving of particles. The wave effect makes a positive contribution to the particles for forming a sandpile with a higher repose angle. Eventually, the irregular-shaped particles exhibit a final repose angle that is noticeably greater than the spherical particles. This phenomenon can be also reflected from the quantitative results of the evolution of particle average velocity with time shown in Fig. 23. The kinetic energy of irregular-shaped particles is less mobilized due to the shape induced resistance between particles, comparing with spherical particles.

The SDF-CFD-DEM approach also provides a bunch of functionality of microscopic investigations. For instance, the configuration of contact force chain at the end of the collapse process for the cases of different ambient water conditions are presented in Fig. 24. The case of irregular-shaped particles presents slightly stronger force chains due to the higher stack of particle sandpile.

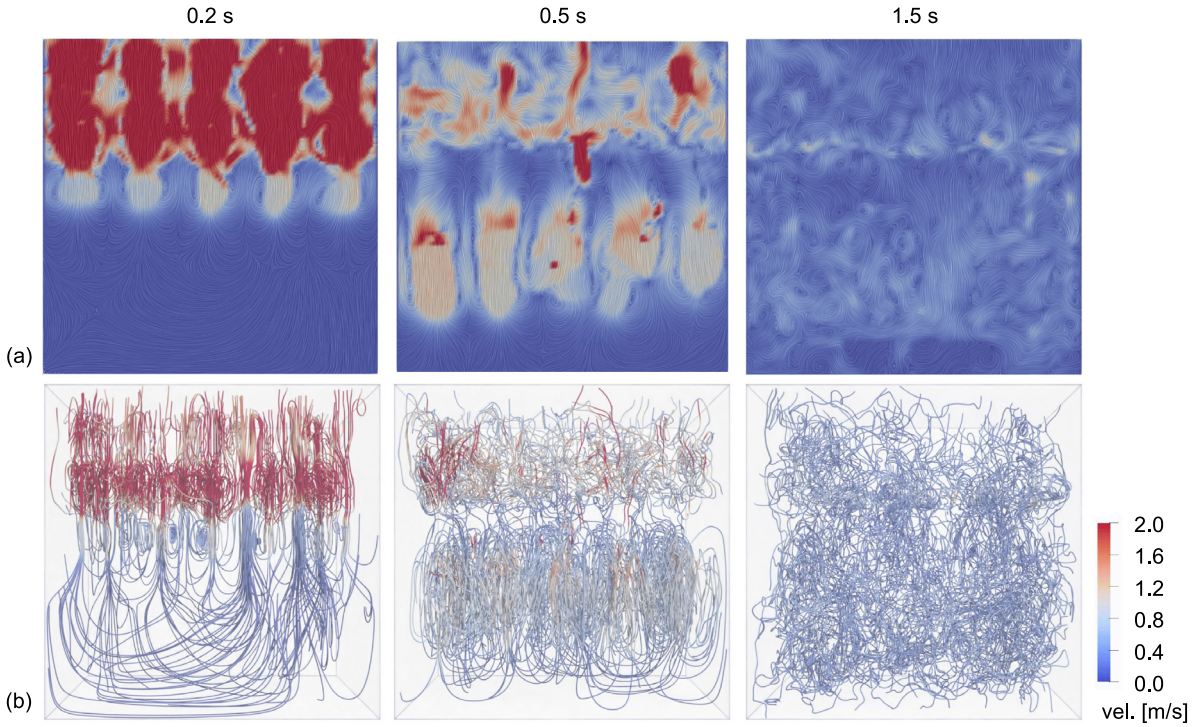

Fig. 20. Velocity contours and streamlines of the fluid field for the example of water entry and settling of various types of particles.

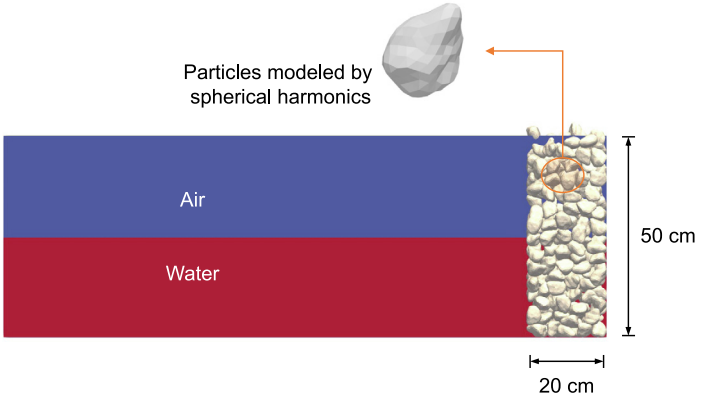

Fig. 21. Setup of the column collapse test on irregular-shaped particles partially under water.

5.4. Mudflow and bedload transport

The last example is about mudflow and bedload transport. As illustrated in Fig. 25, the domain is initialized with air phase, with a sandpile placed at the left lower part of the domain. For the fluid domain, the lower part of left boundary is specified as an inlet to represent an inflow of slurry, and the upper part of the left boundary, top and right boundary are free inlets/outlets depending on the fluid pressure. The model parameters are summarized in Table 3. With the inflow of slurry, the slurry moves forward and interacts with the particles. To gain insights into the effect of inflow velocity on the mudflow-particle interaction, two inlet velocities are considered, namely 0.2 m/s and 1.0 m/s. The simulation lasts for 6.0 s.

To begin with, the snapshots of the mudflow and bedload transport simulation at different time are gathered in Fig. 26. For the case of low inflow velocity, the slurry would gradually climb up the sandpile and then flow

Table 2
Model parameters of the column collapse example.

Domain	Properties	Values
CFD	Domain size	150 cm × 20 cm × 50 cm
	Discretization	225 × 30 × 75 cells
	Density of water	1000 kg/m^3
	Viscosity of water	1.0e−6 m^2/s
	Density of air	1.2 kg/m^3
	Viscosity of air	1.48e−5 m^2/s
	Surface tension coefficient	0.07
	Timestep	Adaptive
DEM	Number of particles	320
	Particle size	3.86 cm
	Particle density	2600 kg/m^3
	Contact normal stiffness	2.0e5 N/m
	Contact tangential stiffness	1.0e5 N/m
	Contact friction coefficient	0.5
	Contact damping coefficient	0.7
	Timestep	1.0e−4 s

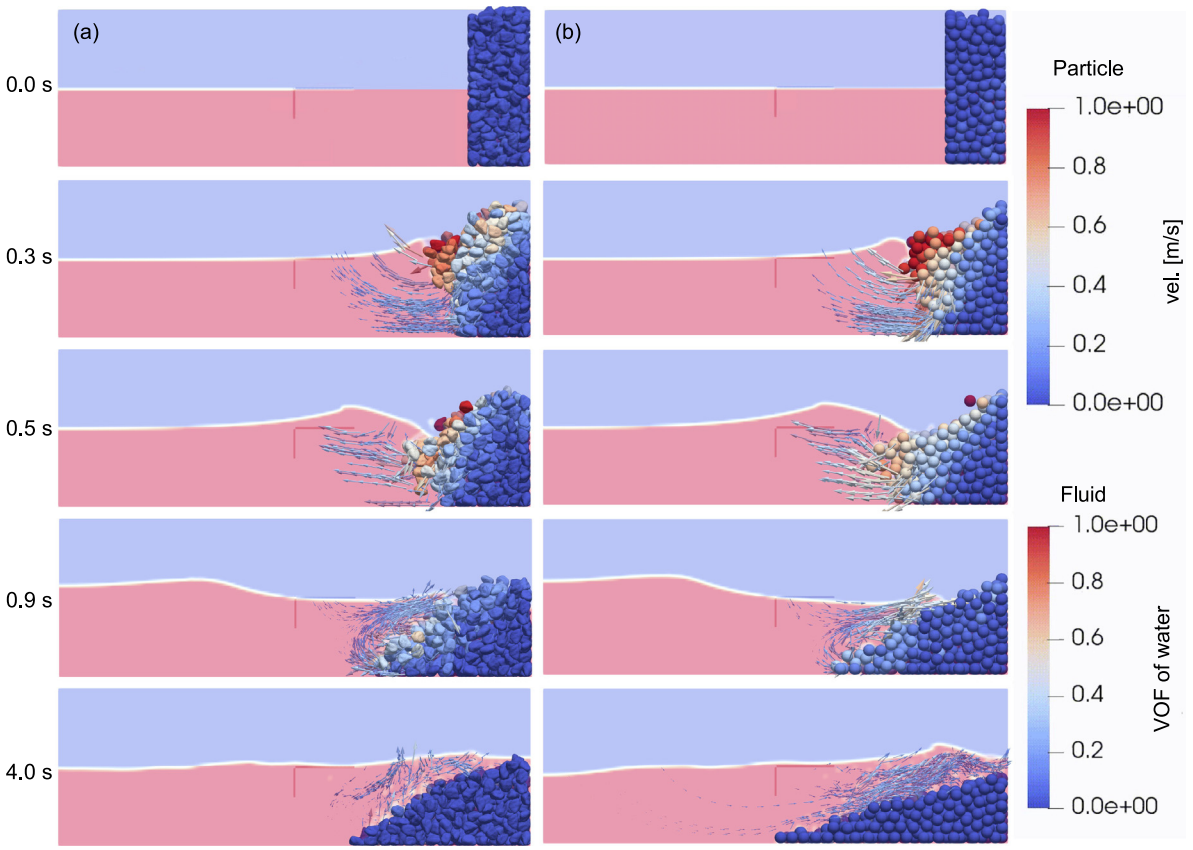

Fig. 22. Snapshots of column collapse of (a) irregular-shaped particles and (b) spherical particles.

downward along the back side of the sandpile. Along with the flow of slurry, the particles at the back side of the sandpile are brought downward and move with the slurry. On the contrary, for the case of high inflow velocity, the slurry flows fast along the front side of the sandpile and creates a small cavity at the back side of the sandpile. The difference in the mudflow behavior due to inlet velocity results in different patterns of particle transport. As

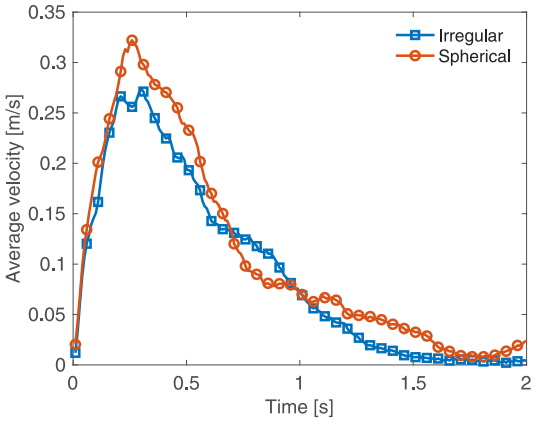

Fig. 23. Evolution of particle average velocity with time during the collapsing process for irregular-shaped and spherical particles.

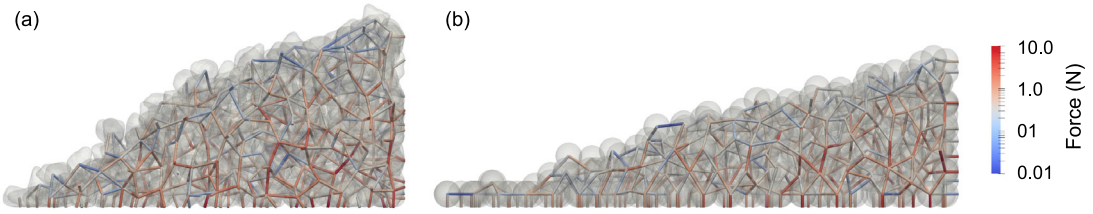

Fig. 24. Configurations of contact force chain at the end of the collapse process for (a) irregular-shaped and (b) spherical particles.

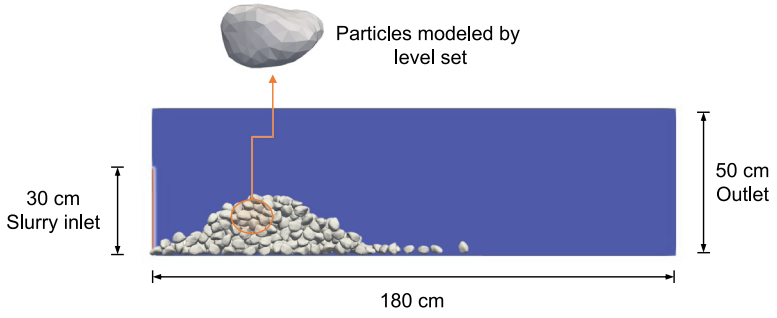

Fig. 25. Simulation setup of the mudflow and bedload transport example.

illustrated in Fig. 27 with cut-plane views, particles at the back side are subjected to high erosion for the case of low inlet velocity, whereas the opposite for the case of high inlet velocity. The complex interaction between slurry and particle in mudflow and bedload transport is well recaptured by the SDF-CFD-DEM simulation.

To gain insights into the movement of particles after erosion, the trajectories of the particles during the whole simulation are extracted and plotted in Fig. 28. For the case of low inlet velocity, it is at the back side of the sandpile where most of the particles are mobilized and moved with the mudflow; whereas for the case of high inlet velocity, the particles at the front side are first mobilized and thus their early-stage trajectories exhibit a mountain-like profile. It should be noted that the present simulation represents a simplified case of mudflow and bedload transport to demonstrate the capability of the SDF-CFD-DEM for modeling the complex interaction between fluid and irregular-shaped particles. It can be expanded to realistic problems with more complex model geometries, viscous models, and boundary conditions in future.

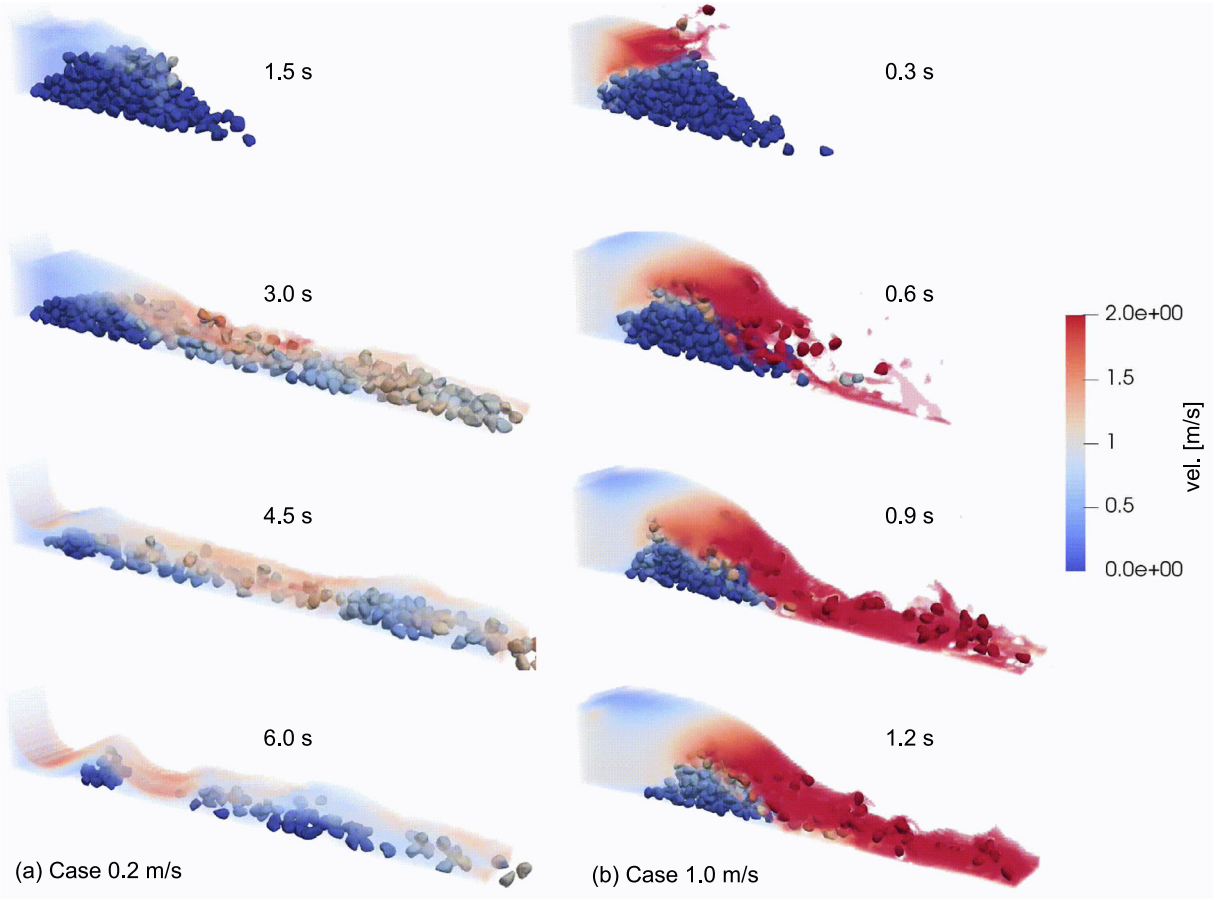

Fig. 26. Snapshots of mudflow and transport of irregular-shaped particles: (a) inlet velocity of 0.2 m/s and (b) inlet velocity of 1.0 m/s.

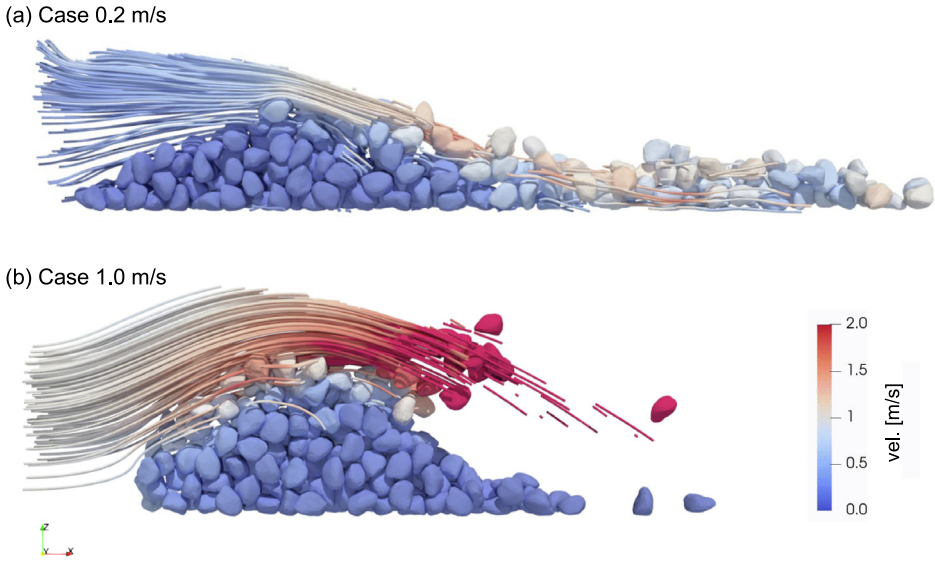

Fig. 27. Illustration of particle transport patterns for different mudflow velocities: (a) case 0.2 m/s at time 2.5 s and (b) case 1.0 m/s at time 0.5 s.

Table 3
Model parameters of the mudflow and bedload transport example.

Domain	Properties	Values
CFD	Domain size	180 cm × 20 cm × 50 cm
	Discretization	270 × 30 × 75 cells
	Density of slurry	1600 kg/m^3
	Viscosity of slurry	1.0e−4 m^2/s
	Density of air	1.2 kg/m^3
	Viscosity of air	1.48e−5 m^2/s
	Surface tension coefficient	0.07
	Timestep	Adaptive
DEM	Number of particles	320
	Particle size	3.86 cm
	Particle density	2600 kg/m^3
	Contact normal stiffness	2.0e5 N/m
	Contact tangential stiffness	1.0e5 N/m
	Contact friction coefficient	0.5
	Contact damping coefficient	0.7
	Timestep	1.0e−4 s

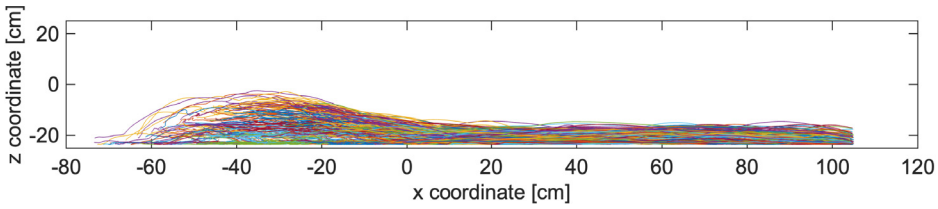

(a) Inlet velocity of 0.2 m/s

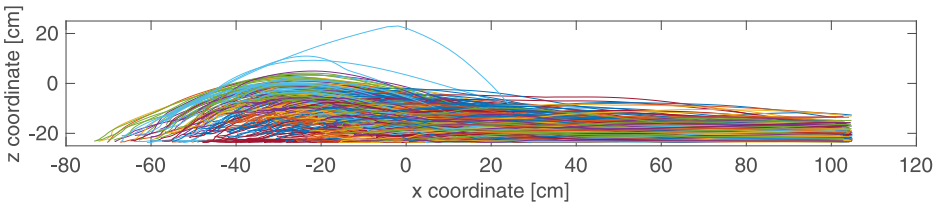

(b) Inlet velocity of 1.0 m/s

Fig. 28. Particle trajectory during the transport process: (a) inlet velocity of 0.2 m/s and (b) inlet velocity of 1.0 m/s.

6. Summary

This paper presented a signed distance field (SDF)-based CFD-DEM for numerical modeling of multiphase fluids and arbitrary-shaped particles. It solves the interaction between fluids and particles in a fully resolved manner by adopting the immersed boundary method (IBM). An attractive feature of the proposed SDF-CFD-DEM is that it integrates the SDF-DEM for computational particle dynamics, which renders it flexible and efficient to model any types of irregular-shaped particles. In addition, the contact potential based energy conservative contact theory is adopted to resolve the contact behavior between arbitrary-shaped particles, which enables quantitative energy analysis of a CFD-DEM simulation. For mapping DEM particles onto CFD domain, an SDF-based solid fraction estimation approach is proposed and its accuracy for various types of particles has been demonstrated. Results of verification examples including particle settling test and drafting–kissing–tumbling test have demonstrated the good accuracy of the proposed SDF-CFD-DEM. Illustrative examples of collision and energy evolution of irregular-shaped particles, water entry of various types of particles, immersed granular collapse and bedload transport have further showcased the capability of the SDF-CFD-DEM in modeling complex fluid and granular flow with irregular-shaped particles. The proposed SDF-based CFD-DEM would help to unleash the strengths of computational particle

mechanics involving irregular shapes and become an efficient and robust tool for exploring complex fluid–particle interactions in a fully resolved sense to improve our understanding on how particle shape irregularity interplays with the mechanical response of fluid for granular flows.

Declaration of competing interest

The authors declare that they have no known competing financial interests or personal relationships that could have appeared to influence the work reported in this paper.

Data availability

Data will be made available on request.

Acknowledgments

This work was financially supported by the Hong Kong Scholars Program (2020), the Research Grants Council of Hong Kong (16208720, F-HKUST601/19), the National Natural Science Foundation of China (51909289, 51978677), the Shenzhen Science and Technology Project for Sustainable Development (KCXFZ202002011008532, KCXFZ20201221173207020), and the Project of Hetao Shenzhen-Hong Kong Science and Technology Innovation Cooperation Zone (HZQBKCZYB2020083). The study was also partially supported by HKUST internal research supports (FP907, IEG22EG01).

Appendix. Formulation of a linear contact potential

As an analogy of linear contact model, the linear contact potential for the SDF-DEM is taken as

$$w(\boldsymbol{x}, \boldsymbol{\theta}) = \frac{2k_n \mathcal{S}(d_i) S_B d_i}{\pi N_B d_B} \tag{A.1}$$

where k_n is the equivalent normal stiffness, d_i is the signed distance of intruding node i, and S_B, N_B and d_B are the surface area, number of surface nodes and equivalent size of particle B, respectively. $\mathcal{S}(d_i)$ is a sigmoid function that satisfies $\mathcal{S}(0) = 0$ and $\mathcal{S}(d_{i,\max}) = 1$, and $d_{i,\max}$ represents the maximum permissible intrusion depth during a collision event. For the small contact theory in DEM, $d_{i,\max}$ is usually less than 5% of particle size. The sigmoid function implies that the contact volume associated with intruding node N_i is counted as zero when this node just starts to intrude into Particle A (i.e., $d_i = 0$), and is totally counted if the intruding depth become significant (i.e., $d_i = d_{i,\max}$). In this work, the following algebraic formulation of sigmoid function is adopted due to its computational efficiency

$$\mathcal{S}(d_i) = \frac{c_s d_i / d_B}{\sqrt{1 + (c d_i / d_B)^2}} \tag{A.2}$$

where c_s is a constant parameter that controls the shape of function, which is estimated by $c_s = 100$.

References

[1] D. Peng, L. Zhang, R. Jiang, S. Zhang, P. Shen, W. Lu, X. He, Initiation mechanisms and dynamics of a debris flow originated from debris-ice mixture slope failure in southeast Tibet, China, Eng. Geol. (2022) 106783.

[2] R. Fell, C.F. Wan, J. Cyganiewicz, M. Foster, Time for development of internal erosion and piping in embankment dams, J. Geotech. Geoenviron. Eng. 129 (4) (2003) 307–314.

[3] J.P. den Bieman, M.R.A. van Gent, B.M. Hoonhout, Physical model of scour at the toe of rock armoured structures, Coast. Eng. 154 (2019) 103572.

[4] X. Wang, Y. Wu, J. Cui, C. Zhu, X. Wang, Shape characteristics of coral sand from the south China sea, J. Mar. Sci. Eng. 8 (10) (2020) 803.

[5] L. Huilin, H. Yurong, D. Gidaspow, Y. Lidan, Q. Yukun, Size segregation of binary mixture of solids in bubbling fluidized beds, Powder Technol. 134 (1–2) (2003) 86–97.

[6] L. Huang, J. Ma, M. Lei, L. Liu, Y. Lin, Z. Zhang, Soil-water inrush induced shield tunnel lining damage and its stabilization: A case study, Tunnelling and Underground Space Technology 97 (2020) 103290.

[7] H. Xiong, H. Wu, X. Bao, J. Fei, Investigating effect of particle shape on suffusion by CFD-DEM modeling, Constr. Build. Mater. 289 (2021) 123043.

[8] Y. Lin, X. Wang, J. Ma, L. Huang, A systematic approach for modelling the hydraulic fracturing of rocks with irregular inclusions using a combined finite-discrete method, Eng. Fracture Mech. 261 (2022) 108209.
[9] R. Temam, Navier-Stokes Equations: Theory and Numerical Analysis, Volume 343, American Mathematical Soc. 2001.
[10] F. Moukalled, L. Mangani, M. Darwish, The finite volume method, in: The Finite Volume Method in Computational Fluid Dynamics, Springer, 2016, pp. 103–135.
[11] R. Löhner, Applied Computational Fluid Dynamics Techniques: An Introduction Based on Finite Element Methods, John Wiley & Sons, 2008.
[12] C. Shu, High-order finite difference and finite volume WENO schemes and discontinuous Galerkin methods for CFD, Int. J. Comput. Fluid Dyn. 17 (2) (2003) 107–118.
[13] S. Chen, G.D. Doolen, Lattice Boltzmann method for fluid flows, Annu. Rev. Fluid Mech. 30 (1) (1998) 329–364.
[14] J.J. Monaghan, Smoothed particle hydrodynamics, Annu. Rev. Astron. Astrophys. 30 (1992) 543–574.
[15] H. Jasak, A. Jemcov, Z. Tukovic, et al., OpenFOAM: A C++ library for complex physics simulations, in: International Workshop on Coupled Methods in Numerical Dynamics, Volume 1000, IUC Dubrovnik Croatia, 2007, pp. 1–20.
[16] J. Latt, O. Malaspinas, D. Kontaxakis, A. Parmigiani, D. Lagrava, F. Brogi, M.B. Belgacem, Y. Thorimbert, S. Leclaire, S. Li, et al., Palabos: parallel lattice Boltzmann solver, Comput. Math. Appl. 81 (2021) 334–350.
[17] A.J. Crespo, J.M. Domínguez, B.D. Rogers, M. Gómez-Gesteira, S. Longshaw, R. Canelas, R. Vacondio, A. Barreiro, O. García-Feal, DualSPHysics: Open-source parallel CFD solver based on smoothed particle hydrodynamics (SPH), Comput. Phys. Comm. 187 (2015) 204–216.
[18] P.A. Cundall, O.D.L. Strack, A discrete numerical model for granular assemblies, Géotechnique 29 (1) (1979) 47–65.
[19] P.W. Cleary, M.L. Sawley, DEM modelling of industrial granular flows: 3D case studies and the effect of particle shape on hopper discharge, Appl. Math. Model. 26 (2) (2002) 89–111.
[20] H.P. Zhu, Z.Y. Zhou, R.Y. Yang, A.B. Yu, Discrete particle simulation of particulate systems: a review of major applications and findings, Chem. Eng. Sci. 63 (23) (2008) 5728–5770.
[21] A. Lisjak, G. Grasselli, A review of discrete modeling techniques for fracturing processes in discontinuous rock masses, J. Rock Mech. Geotech. Eng. 6 (4) (2014) 301–314.
[22] Y. Xia, J.J. Stickel, W. Jin, J. Klinger, A review of computational models for the flow of milled biomass I: Discrete-particle models, ACS Sustain. Chem. Eng. (2020).
[23] K. Chu, B. Wang, A. Yu, A. Vince, CFD-DEM modelling of multiphase flow in dense medium cyclones, Powder Technol. 193 (3) (2009) 235–247.
[24] J. Zhao, T. Shan, Coupled CFD–DEM simulation of fluid–particle interaction in geomechanics, Powder Technol. 239 (2013) 248–258.
[25] Y. Guo, X.B. Yu, Comparison of the implementation of three common types of coupled CFD-DEM model for simulating soil surface erosion, Int. J. Multiph. Flow. 91 (2017) 89–100.
[26] L. Lu, X. Gao, M. Shahnam, W.A. Rogers, Simulations of biomass pyrolysis using glued-sphere CFD-DEM with 3-D intra-particle models, Chem. Eng. J. 419 (2021) 129564.
[27] S. McIntyre, M. Kinzel, S. Miller, E. Paterson, J. Lindau, R. Kunz, The immersed boundary method for water entry simulation, in: 49th AIAA Aerospace Sciences Meeting Including the New Horizons Forum and Aerospace Exposition, 2011, p. 759.
[28] M. Wang, Y.T. Feng, D.R.J. Owen, T.M. Qu, A novel algorithm of immersed moving boundary scheme for fluid–particle interactions in DEM–LBM, Comput. Methods Appl. Mech. Engrg. 346 (2019) 109–125.
[29] Y. Zhang, G. Pan, Y. Zhang, S. Haeri, A multi-physics peridynamics-DEM-IB-CLBM framework for the prediction of erosive impact of solid particles in viscous fluids, Comput. Methods Appl. Mech. Engrg. 352 (2019) 675–690.
[30] J. Mao, L. Zhao, Y. Di, X. Liu, W. Xu, A resolved CFD–DEM approach for the simulation of landslides and impulse waves, Comput. Methods Appl. Mech. Engrg. 359 (2020) 112750.
[31] T. Yu, J. Zhao, Semi-coupled resolved CFD–DEM simulation of powder-based selective laser melting for additive manufacturing, Comput. Methods Appl. Mech. Engrg. 377 (2021) 113707.
[32] X. Nan, J. Hou, Z. Shen, Y. Tong, G. Li, X. Wang, Y. Kang, CFD-DEM coupling with multi-sphere particles and application in predicting dynamic behaviors of drifting boats, Ocean Eng. 247 (2022) 110368.
[33] A.N. Balachandran Nair, S. Pirker, M. Saeedipour, Resolved CFD-DEM simulation of blood flow with a reduced-order RBC model, Comput. Part. Mech. 9 (4) (2022) 759–774.
[34] P.P. Brown, D.F. Lawler, Sphere drag and settling velocity revisited, J. Environ. Eng. 129 (3) (2003) 222–231.
[35] E. Loth, Drag of non-spherical solid particles of regular and irregular shape, Powder Technol. 182 (3) (2008) 342–353.
[36] Z. Wang, M. Liu, Semi-resolved CFD–DEM for thermal particulate flows with applications to fluidized beds, Int. J. Heat Mass Transfer 159 (2020) 120150.
[37] H.H. Hu, N.A. Patankar, M.Y. Zhu, Direct numerical simulations of fluid–solid systems using the arbitrary Lagrangian–Eulerian technique, J. Comput. Phys. 169 (2) (2001) 427–462.
[38] C.S. Peskin, Flow patterns around heart valves: a numerical method, J. Comput. Phys. 10 (2) (1972) 252–271.
[39] G.C. Cho, J. Dodds, J.C. Santamarina, Particle shape effects on packing density, stiffness, and strength: natural and crushed sands, J. Geotech. Geoenviron. Eng. 132 (5) (2006) 591–602.
[40] W. Xiao, H. Zhang, K. Luo, C. Mao, J. Fan, Immersed boundary method for multiphase transport phenomena, Rev. Chem. Eng. (2020).
[41] H. Ma, L. Zhou, Z. Liu, M. Chen, X. Xia, Y. Zhao, A review of recent development for the CFD-DEM investigations of non-spherical particles, Powder Technol. (2022) 117972.
[42] S.A. Galindo-Torres, A coupled discrete element lattice Boltzmann method for the simulation of fluid–solid interaction with particles of general shapes, Comput. Methods Appl. Mech. Engrg. 265 (2013) 107–119.

[43] M. Wang, Y.T. Feng, T.M. Qu, T.T. Zhao, A coupled polygonal DEM-LBM technique based on an immersed boundary method and energy-conserving contact algorithm, Powder Technol. 381 (2021) 101–109.
[44] X. Zhang, P. Tahmasebi, Coupling irregular particles and fluid: Complex dynamics of granular flows, Comput. Geotech. 143 (2022) 104624.
[45] X. Zhang, P. Tahmasebi, Investigation of particle shape and ambient fluid on sandpiles using a coupled micro-geomechanical model, Powder Technol. (2022) 117711.
[46] N. Das, Modeling Three-Dimensional Shape of Sand Grains Using Discrete Element Method (Ph.D. thesis), University of South Florida, 2007.
[47] Z. Shen, G. Wang, D. Huang, F. Jin, A resolved CFD-DEM coupling model for modeling two-phase fluids interaction with irregularly shaped particles, J. Comput. Phys. 448 (2022) 110695.
[48] C.M. Pereira, A.L. Ramalho, J.A. Ambrósio, A critical overview of internal and external cylinder contact force models, Nonlinear Dynam. 63 (4) (2011) 681–697.
[49] H.A. Navarro, M.P. de Souza Braun, Determination of the normal spring stiffness coefficient in the linear spring–dashpot contact model of discrete element method, Powder Technol. 246 (2013) 707–722.
[50] Z. Lai, S. Zhao, J. Zhao, L. Huang, Signed distance field framework for unified DEM modeling of granular media with arbitrary particle shapes, Comput. Mech. 70 (2022) 763–783.
[51] R. Kawamoto, E. Andò, G. Viggiani, J.E. Andrade, Level set discrete element method for three-dimensional computations with triaxial case study, J. Mech. Phys. Solids 91 (2016) 1–13.
[52] B. Zhou, J. Wang, Generation of a realistic 3D sand assembly using X-ray micro-computed tomography and spherical harmonic-based principal component analysis, Int. J. Numer. Anal. Methods Geomech. 41 (1) (2017) 93–109.
[53] C. Zhang, sdfibm: a signed distance field based discrete forcing immersed boundary method in OpenFOAM, Comput. Phys. Comm. 255 (2020) 107370.
[54] J. Roenby, H. Bredmose, H. Jasak, IsoAdvector: Geometric VOF on general meshes, in: OpenFOAM®, Springer, 2019, pp. 281–296.
[55] Y.T. Feng, An energy-conserving contact theory for discrete element modelling of arbitrarily shaped particles: Basic framework and general contact model, Comput. Methods Appl. Mech. Engrg. 373 (2021) 113454.
[56] K.L. Johnson, Contact Mechanics, Cambridge University Press, 1987.
[57] R. Balevičius, Z. Mróz, A finite sliding model of two identical spheres under displacement and force control – part I: static analysis, Acta Mech. 224 (8) (2013) 1659–1684.
[58] T. Kajishima, S. Takiguchi, H. Hamasaki, Y. Miyake, Turbulence structure of particle-laden flow in a vertical plane channel due to vortex shedding, JSME Int. J. B 44 (4) (2001) 526–535.
[59] B. Bigot, T. Bonometti, L. Lacaze, O. Thual, A simple immersed-boundary method for solid–fluid interaction in constant-and stratified-density flows, Comput. & Fluids 97 (2014) 126–142.
[60] A.A. Shirgaonkar, M.A. Maciver, N.A. Patankar, A new mathematical formulation and fast algorithm for fully resolved simulation of self-propulsion, J. Comput. Phys. 228 (7) (2009) 2366–2390.
[61] J. Yang, E. Balaras, An embedded-boundary formulation for large-eddy simulation of turbulent flows interacting with moving boundaries, J. Comput. Phys. 215 (1) (2006) 12–40.
[62] W.P. Breugem, A second-order accurate immersed boundary method for fully resolved simulations of particle-laden flows, J. Comput. Phys. 231 (13) (2012) 4469–4498.
[63] S.V. Apte, M. Martin, N.A. Patankar, A numerical method for fully resolved simulation (FRS) of rigid particle–flow interactions in complex flows, J. Comput. Phys. 228 (8) (2009) 2712–2738.
[64] T. Kempe, J. FröHlich, An improved immersed boundary method with direct forcing for the simulation of particle laden flows, J. Comput. Phys. 231 (9) (2012) 3663–3684.
[65] B. Blais, M. Lassaigne, C. Goniva, L. Fradette, F. Bertrand, A semi-implicit immersed boundary method and its application to viscous mixing, Comput. Chem. Eng. 85 (2016) 136–146.
[66] P.G. Tucker, Differential equation-based wall distance computation for DES and RANS, J. Comput. Phys. 190 (1) (2003) 229–248.
[67] D.K. Kolmogorov, Numerical aspects of wall-distance computation for turbulence modeling, in: Journal of Physics: Conference Series, Volume 1400, IOP Publishing, 2019, 044037.
[68] E. Attar, Simulation of Selective Electron Beam Melting Processes, Friedrich-Alexander-Universitaet Erlangen-Nuernberg (Germany), 2011.
[69] R.I. Issa, Solution of the implicitly discretised fluid flow equations by operator-splitting, J. Comput. Phys. 62 (1) (1986) 40–65.
[70] A. ten Cate, C.H. Nieuwstad, J.J. Derksen, H.E.A. Van den Akker, Particle imaging velocimetry experiments and lattice-Boltzmann simulations on a single sphere settling under gravity, Phys. Fluids 14 (11) (2002) 4012–4025.
[71] M. Fan, D. Su, L. Yang, Development of a benchmark for drag correlations of nonspherical particles based on settling experiments of super-ellipsoidal particles, Powder Technol. 409 (2022) 117811.
[72] A.F. Fortes, D.D. Joseph, T.S. Lundgren, Nonlinear mechanics of fluidization of beds of spherical particles, J. Fluid Mech. 177 (1987) 467–483.
[73] R. Glowinski, T.W. Pan, T.I. Hesla, D.D. Joseph, J. Periaux, A fictitious domain approach to the direct numerical simulation of incompressible viscous flow past moving rigid bodies: application to particulate flow, J. Comput. Phys. 169 (2) (2001) 363–426.
[74] Y. Yang, S. Balachandar, A scalable parallel algorithm for direct-forcing immersed boundary method for multiphase flow simulation on spectral elements, J. Supercomput. 77 (2021) 2897–2927.
[75] P. Gondret, M. Lance, L. Petit, Bouncing motion of spherical particles in fluids, Phys. Fluids 14 (2) (2002) 643–652.
[76] P. Costa, B.J. Boersma, J. Westerweel, W.P. Breugem, Collision model for fully resolved simulations of flows laden with finite-size particles, Phys. Rev. E 92 (5) (2015) 053012.